Composite Structures 353 (2025) 118697

Contents lists available at ScienceDirect

Composite Structures

journal homepage: www.elsevier.com/locate/compstruct

A DG-VLM framework for computational static aeroelastic analysis of composite wings

Dario Campagna [a], Vincenzo Gulizzi [a,b,*], Ivano Benedetti [a]

[a] Department of Engineering, Università degli Studi di Palermo, Italy
[b] Istituto Nazionale di Alta Matematica, Gruppo Nazionale per la Fisica Matematica, Italy

ARTICLE INFO

Keywords:
Computational aeroelasticity
Aeroelastic divergence
Multi-layered composite plates
Discontinuous Galerkin method
Vortex lattice method

ABSTRACT

A computational framework for static aeroelastic analysis of composite laminated plates is proposed, whose novelty is the conjoined use of a structural discontinuous Galerkin (DG) formulation and an aerodynamic vortex lattice method (VLM), suitably coupled for the monolithic solution of the aeroelastic problem. The structural method is built on variable-order generalized kinematics, which allows the seamless adoption of either beam or plate modeling strategies, with on-demand order of polynomial approximation over the transverse and in-plane dimensions of the structural elements. The underlying DG formulation also simplifies the coupling between the structural and aerodynamic grids, thus providing a versatile tool for the aeroelastic analysis of either low or high aspect-ratio composite wings. Several numerical tests have been performed to assess the convergence features of the proposed framework as well as its accuracy with respect to available computational and experimental benchmark data. The obtained results confirm its robustness and highlight its potential for aeroelastic assessments in early aircraft conceptual design.

1. Introduction

Aeroelasticity, which lies at the intersection between structural mechanics and aerodynamics, plays an important role in several fields of engineering, providing enabling technologies for the realization of large civil infrastructures, such as long-span suspension bridges and high-rise buildings [1,2], aircraft and aerospace structures [3–5], turbo-machinery components [6], and energy harvesting devices, including small-scale piezoelectric harvesters [7] as well as large-scale and off-shore wind turbines [8–11], among other applications.

Composite materials have consolidated their role in high-performance structural applications and are today widely employed in the automotive and aerospace industries, as they deliver high stiffness and strength at low weight, which is of interest for energy efficient transportation. Additionally, leveraging on a wide design space in terms of base materials selection and architecture (matrix, fibers, stacking sequence), they offer the opportunity to tailor the material manufacturing and internal architecture on the specific application, e.g. optimizing stiffness along specific directions in accordance with the considered load paths, thus promoting structural performance and efficiency. As exemplified by the development of the *Grumman* X-29, anisotropic elastic couplings between bending and twisting in carbon fiber reinforced composite plates and shells can be profitably exploited to delay or avoid aeroelastic divergence in innovative aircraft configurations, in the context of the so-called *aeroelastic tailoring* [12–14]. Aeroelastic tailoring, implemented through composite structures, is gathering renewed relevance in the framework of emerging aerospace technologies for green aviation, which consistently include the employment of high-aspect-ratio wings for enhanced aerodynamic efficiency [15]. Indeed, high-aspect-ratio wings tend to suffer from the effects of high flexibility, which may promote aeroelastic divergence and flutter [16].

The above considerations motivate the interest in the development of reliable tools for conceptual and preliminary analysis of aircraft architectures. In the literature, several formulations and methods have been proposed for the analysis of the aeroelastic behavior of composite aircraft structures [17–19]. Beyond specific technical aspects, the adopted formulations may differ for the level of fidelity retained in the analysis, ranging from high-resolution models coupling computational structural dynamics (CSD) with sophisticated computational fluids dynamics (CFD) [20–24] to more simplified representations, where either the structural response [25,26], the aerodynamic response [27], or both the structure and aerodynamic fields are reconstructed using simplified models, such as aerodynamic potential flow theories or structural beam theories [28–36], which are typically able to capture the main features and trends of the considered problem. The development and

* Corresponding author at: Department of Engineering, Università degli Studi di Palermo, Italy.
E-mail addresses: vincenzo.gulizzi@unipa.it (V. Gulizzi), ivano.benedetti@unipa.it (I. Benedetti).

https://doi.org/10.1016/j.compstruct.2024.118697
Received 9 July 2024; Received in revised form 24 September 2024; Accepted 8 November 2024
Available online 18 November 2024

practical employment of high-fidelity models is hindered by the high computational costs attracted by such kinds of analysis, entailing the coupled resolution of structural and fluids fields, which is the reason why considerable efforts are devoted to the development of reduced order modeling (ROM) strategies for aeroelastic analysis [37–39].

Although high-fidelity models, including the detailed representation of structural and aerodynamic features, are certainly useful in advanced stages of design, where they can complement pre-production experimental assessments,fine-tuning or post-production adjustments, there is relevant interest in fast and sufficiently accurate and reliable computational tools to assist in the selection between alternative structural or architectural configurations during conceptual design development, when several alternatives need to be assessed before focusing on the fewer most promising ones.

In this contribution we propose an original computational framework for the static aeroelastic analysis of multi-layered composite plates based on the conjoined use of a discontinuous Galerkin (DG) method for structural analysis and a vortex lattice method (VLM) for the resolution of the aerodynamic field and forces, coupled through an interface ensuring the consistence between aerodynamic loads and structural deflections. Unlike similar solution strategies for solving partial differential equations, such as the Finite Element Method (FEM), the key feature of DG-based formulations is the use of a space of discontinuous basis functions and suitably defined boundary integrals to weakly enforce boundary and interface conditions, including the continuity of the solution between adjacent elements. The discontinuous nature of the basis functions allows enabling high-order accuracy for conventional and non-conventional (e.g. polytopic) meshes, simplifying the coupling between elements featuring different orders of approximation or different mathematical models in multi-physics problems, making the method amenable to massive parallelization. With regards to the considered aeroelastic problems, the strength of the method lies in the versatility of the underlying kinematic structural model, which offers the possibility of adapting the order of approximation of the unknown fields, so to capture complex in-plane and through-the-thickness kinematic and static patterns, and in the seamless coupling with the adopted aerodynamic model. While the benefits of the DG-VLM coupling for aeroelastic analysis had been first explored in Ref. [36], the novelty of the present contribution consists in proposing, implementing, testing and validating the framework for the analysis of general *composite multi-layer* plates, which is of relevant interest in the context of aeroelastic tailoring for aerospace applications.

The paper is organized as follows. Section 2 describes the basic features of the analyzed aeroelastic problem, specifying the reference geometry and providing some background information about the structural and aerodynamic grids employed in the computations. Section 3 details the proposed structural model, from the kinematic assumptions and associated constitutive relationships to the DG weak form employed for its solution. Section 4 recalls the main features of the selected VLM aerodynamic model, based on potential flow theory. Section 5 explains how the coupling between the structural model and the aerodynamic model is implemented, highlighting the assumptions that allow the monolithic solution of the considered fluid–structure interaction problem. Section 6 presents and discusses the sets of numerical tests considered for validating the developed framework. Eventually, Section 7 critically discusses the main features of the proposed method and identify potential directions for further investigation and development, before drawing some summary *Conclusions*.

2. Aeroelastic problem description

This section identifies the class of considered aeroelastic problems and provides some common background information for the developed formulation.

2.1. Geometry and material properties

The considered class of aeroelastic problems is schematically represented in Fig. 1. General rectangular wings with reference surface S, wingspan b, airfoils chord c, and sweep angle Λ are considered. The wings are described using a global reference system $Ox_1x_2x_3$ centered at the quarter chord of the root section with: the axis x_1 contained in the plane of symmetry of the wing, aligned with the root chord and pointing towards the leading edge; the axis x_3 perpendicular to the axis x_1, lying on the plane of symmetry of the wing, and oriented towards the wing pressure side; and the axis x_2 orthogonal to the plane of symmetry and oriented so to define a right-handed reference system together with the axes x_1 and x_3, see Figs. 1–2. The free-stream aerodynamic speed V_∞ is oriented so to identify the angle of attack α with respect to the axis x_1.

From the structural point of view, flat multilayered plates are considered. The generic wing plate has thickness ζ and it is assembled from a number N_ℓ of laminae or layers; each lamina ℓ has thickness $\zeta^{\langle\ell\rangle}$ and features unidirectional fibers aligned along the local material axis $\widetilde{x}_1^{\langle\ell\rangle}$, defined so that $\widetilde{x}_1^{\langle\ell\rangle}$ forms an angle $\theta^{\langle\ell\rangle}$ with the global reference axis x_1 and $\widetilde{x}_3^{\langle\ell\rangle}$ coincides with the global reference axis x_3, as shown in Fig. 1(b).

The geometry of the problem is described by parametric coordinates ξ_1, ξ_2, and ξ_3 running along the chord, span, and thickness of the considered wing, respectively. In particular, a generic point $\boldsymbol{x} = \boldsymbol{x}(\boldsymbol{\xi})$, with $\boldsymbol{\xi} \equiv (\xi_1, \xi_2, \xi_3)$, belonging to the wing volume is constructed as follows: let $\boldsymbol{x}_R$ and $\boldsymbol{x}_T$ be the locations of the quarter-chord points of the root section and of the tip section, respectively, such that a point $\boldsymbol{x}_{c/4}$ on the quarter-chord line of the wing can be expressed as

$$\boldsymbol{x}_{c/4}(\xi_2) = \boldsymbol{x}_R + (\boldsymbol{x}_T - \boldsymbol{x}_R)\xi_2, \tag{1}$$

where $\xi_2 \in [0, 1]$. It is worth noting that, for the case in Fig. 1(a), $\boldsymbol{x}_R = \boldsymbol{0}$; however, the formulation is intended to allow also more general parameterizations. Then, a generic point $\boldsymbol{x}_0$ on the mean surface of the wing structure is given by

$$\boldsymbol{x}_0(\xi_1, \xi_2) = \boldsymbol{x}_{c/4}(\xi_2) + (c/4 - \xi_1)\widehat{\boldsymbol{\imath}}, \tag{2}$$

where $\xi_1 \in [0, c]$ and $\widehat{\boldsymbol{\imath}} = (1, 0, 0)^\intercal$. Eventually, the expression of $\boldsymbol{x}$ reads

$$\boldsymbol{x}(\xi_1, \xi_2, \xi_3) = \boldsymbol{x}_0(\xi_1, \xi_2) + \xi_3\, \widehat{\boldsymbol{n}} \tag{3}$$

where $\xi_3 \in [-\zeta/2, \zeta/2]$ and $\widehat{\boldsymbol{n}} \equiv (0, 0, -1)^\intercal$.

2.2. Computational grids

As detailed in the subsequent sections, the numerical treatment of the aeroelastic problem will require a structural mesh and a different aerodynamic mesh, to be suitably coupled for the resolution of the coupled equations. A schematic representation of the adopted computational grids is shown in Fig. 2. The structural mesh is provided by the collection of generic brick elements, which will provide the local supports for the DG formulation. On the other hand, the steady aerodynamic field is addressed employing the VLM, in which a vortex lattice is attached to the plate mean surface, mapped by $\boldsymbol{x}_0(\xi_1, \xi_2)$ in Eq. (2) as $(\xi_1, \xi_2) \in [0, c] \times [0, 1]$, and consists of a grid of ring vortexes plus a row of semi-infinite *horseshoe* vortexes, shed from the wing's trailing edge. As shown in Fig. 2(b), which illustrates the relative arrangement of structural and aerodynamic elements, in general the aerodynamic ring/horseshoe vortexes do not coincide with the structural elements; each ring/horseshoe vortex k is associated with a normal vector $\widehat{\boldsymbol{n}}^k$, which is employed to enforce the aerodynamic flow impenetrability condition at specific control points and will be modified by the deflection of the underlying structure; on the other hand, each vortex element k provides, upon resolution of a generic aerodynamic step, a specific aerodynamic force $\boldsymbol{f}^k$, to be suitably transferred to the underlying structural element for the solution/update of the structural solution. The above description is of general validity, and illustrates

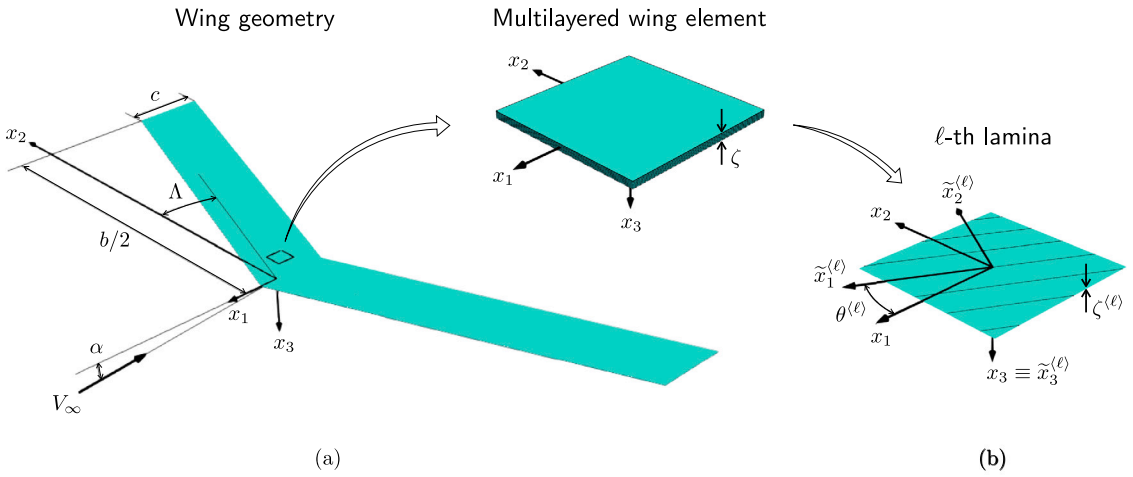

Fig. 1. (a) Geometry of the considered multilayered wing structures; (b) Definition of the local material reference system for the ℓ-th lamina.

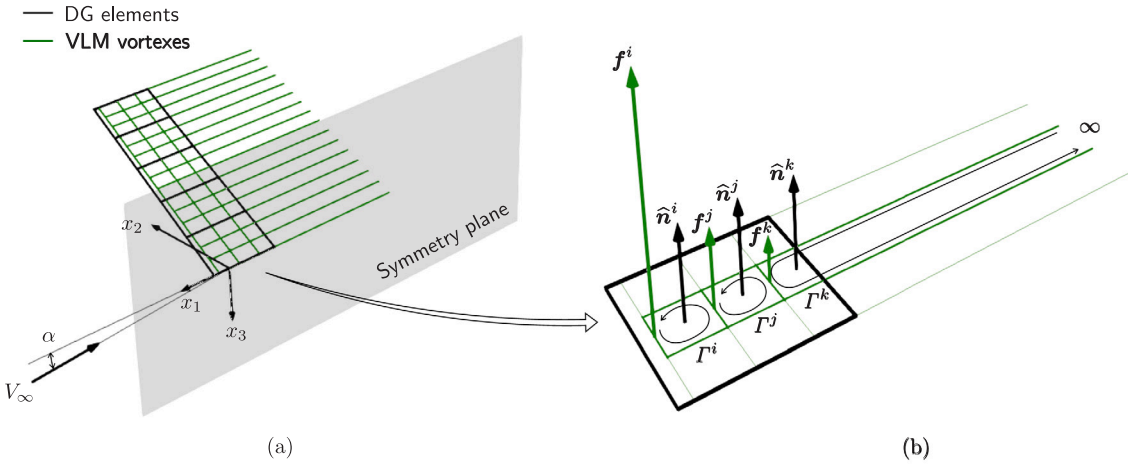

Fig. 2. (a) Discretization of the wing into a collection of structural DG elements (thick black lines) and aerodynamic VLM vortexes (green lines). (b) Closeup of a structural element and of the set of related bound aerodynamic vortexes; a generic ith vortex is associated with the circulation Γ^k, a unit normal vector $\hat{\boldsymbol{n}}^k$ and generates a force $\boldsymbol{f}^k$ on the structural element.

the aeroelastic coupling in general settings in which iterative solution searches are employed; however, in the present work, a monolithic solution approach has been implemented, which provides an equilibrium aeroelastic configuration from the solution of the coupled structural and aerodynamic equations, as it will be detailed in Section 5.

3. Structural model

The wing is assumed to deform under the assumptions of small strains and linear elasticity. The components of the displacement field are collected within the vector $\boldsymbol{u} = (u_1, u_2, u_3)^\intercal$, while the strain and stress components are collected in Voigt ordering and notation within the vectors $\boldsymbol{\gamma} = (\gamma_{11}, \gamma_{22}, \gamma_{33}, \gamma_{23}, \gamma_{31}, \gamma_{12})^\intercal$ and $\boldsymbol{\sigma} = (\sigma_{11}, \sigma_{22}, \sigma_{33}, \sigma_{23}, \sigma_{31}, \sigma_{12})^\intercal$, respectively. The wing is subject to body forces acting over its volume V and surface tractions acting over the portion ∂V_t of its boundary ∂V; the components of the body forces are collected within the vector $\boldsymbol{f} = (f_1, f_2, f_3)^\intercal$, while the components of the surface tractions are collected within $\boldsymbol{t} = (t_1, t_2, t_3)^\intercal$. The wing is also subject to essential boundary conditions $\boldsymbol{u} = \boldsymbol{0}$ for $\boldsymbol{x} \in \partial V_u$ where ∂V_u denotes the root section of the wing, i.e. $\partial V_u \equiv \{\boldsymbol{x} \in V \ : \ x_2 = 0\}$.

The governing equations of the structural problem are derived from the principle of virtual displacements (PVD) for three-dimensional elasticity; for an N_ℓ-layer laminate, the PVD reads

$$\sum_{\ell=1}^{N_\ell} \int_{V^{\langle\ell\rangle}} \delta\boldsymbol{\gamma}^{\langle\ell\rangle\intercal} \boldsymbol{\sigma}^{\langle\ell\rangle} \, \mathrm{d}V = \sum_{\ell=1}^{N_\ell} \int_{V^{\langle\ell\rangle}} \delta\boldsymbol{u}^{\langle\ell\rangle\intercal} \boldsymbol{f}^{\langle\ell\rangle} \, \mathrm{d}V + \sum_{\ell=1}^{N_\ell} \int_{\partial V^{\langle\ell\rangle}} \delta\boldsymbol{u}^{\langle\ell\rangle\intercal} \boldsymbol{t}^{\langle\ell\rangle} \, \mathrm{d}S, \tag{4}$$

where $\delta(\bullet)$ denotes the first variation of the quantity $\bullet$, and the subscript $\langle\ell\rangle$ denotes quantities associated with the ℓ-th lamina. Then, the adoption of different kinematic assumptions on the behavior of the displacement components throughout the wing volume allows obtaining different structural models, see e.g. Ref. [40]. Here, variable-order beam theories (BTs) and variable-order plate theories (PTs) are considered. In both cases, the wing volume V is discretized into a collection of N_e elements, i.e., $V = \bigcup_{e=1}^{N_e} \mathcal{D}^e$, where $\mathcal{D}^e$ is the generic eth element, and the kth displacement component u_k^h is expressed in terms of ξ_1, ξ_2, and ξ_3 as

$$u_k^h(\boldsymbol{x} \in \mathcal{D}^e) = \sum_{i_1=0}^{p_1} \sum_{i_2=0}^{p_2} \sum_{i_3=0}^{p_3} b_{i_1}^e(\xi_1) b_{i_2}^e(\xi_2) b_{i_3}^e(\xi_3) X_{i_1 i_2 i_3}^{e,k} = \sum_{i=1}^{N_p} B_i^e(\xi_1, \xi_2, \xi_3) X_i^{e,k}, \tag{5}$$

where the superscript h indicates that u_k^h is an approximation of the actual displacement component u_k, $b_{i_1}^e(\xi_1)$, $b_{i_2}^e(\xi_2)$, and $b_{i_3}^e(\xi_3)$ denote

the one-dimensional basis functions chosen to express the chord-wise, span-wise, and thickness-wise approximations, respectively, p_1, p_2, and p_3 are the corresponding orders of approximation, and $X^{e,k}_{i_1 i_2 i_3}$ are the associated unknown coefficients. The product $b^e_{i_1}(\xi_1) b^e_{i_2}(\xi_2) b^e_{i_3}(\xi_3)$ can be written as a single basis function $B^e_i(\xi_1, \xi_2, \xi_3)$ of the coordinates ξ_1, ξ_2 and ξ_3, leading to the second equality of Eq. (5), where $X^{e,k}_i$ is the unknown coefficient associated to $B^e_i(\xi_1, \xi_2, \xi_3)$ for the kth displacement component, the index i is associated with the tuple (i_1, i_2, i_3), and $N_p = (1 + p_1)(1 + p_2)(1 + p_3)$. Upon considering the three displacement components, and collecting the unknown coefficients into the $N_u N_p$-dimensional vector $\boldsymbol{X}^e$, with $N_u = 3$, and the basis functions into the $N_u \times N_u N_p$ matrix $\boldsymbol{B}^e$, Eq. (5) may be rewritten in matrix notation as

$$\boldsymbol{u}^h(\boldsymbol{x} \in \mathscr{D}^e) = \boldsymbol{B}^e(\xi_1, \xi_2, \xi_3)\boldsymbol{X}^e. \tag{6}$$

It is worth noting that, in this work, the same expansion orders p_1, p_2, p_3 are associated with the three displacement components, although more general choices could be made, as for example done in the case of the first-order shear deformation theory [41]. BTs and PTs then differ for the wing discretization, kinematic assumptions, and adopted constitutive behavior, as detailed next.

In BTs the wing is discretized using a one-dimensional grid such that the domain $\mathscr{D}^e$ of the generic eth element includes a portion of the wing contained between the two transverse sections identified by $\xi_2 = (e-1)h$ and $\xi_2 = eh$, i.e. $\mathscr{D}^e \equiv [0, c]\times[(e-1)h, eh]\times[-\zeta/2, \zeta/2]$, where $e = 1, \dots, N_e$ and $h \equiv 1/N_e$. Regarding the kinematic assumption, the nth order BT is denoted by BT_n and corresponds to setting $p_1 = p_3 = n$ in Eq. (5), while $p_2 = p$ is varied independently and will identify the order of the chosen DG_p formulation. Eventually, recalling the local material reference systems shown in Fig. 1(b), the stress–strain relationship for a point $\boldsymbol{x}$ lying within the ℓ-th lamina is expressed as

$$\widetilde{\boldsymbol{\sigma}}^{\langle\ell\rangle} = \widetilde{\boldsymbol{c}}^{\langle\ell\rangle}\widetilde{\boldsymbol{\gamma}}^{\langle\ell\rangle}, \tag{7}$$

where $\widetilde{\boldsymbol{\sigma}}^{\langle\ell\rangle}$ and $\widetilde{\boldsymbol{\gamma}}^{\langle\ell\rangle}$ collect the components in the material reference system of the stress and strain tensors, respectively, and the matrix $\widetilde{\boldsymbol{c}}^{\langle\ell\rangle}$ contains the corresponding constitutive constants. Assuming an orthotropic behavior, the $\widetilde{\boldsymbol{c}}^{\langle\ell\rangle}$ is given in terms of the engineering constants as

$$\widetilde{\boldsymbol{c}}^{\langle\ell\rangle} = (\widetilde{\boldsymbol{s}}^{\langle\ell\rangle})^{-1} \quad \text{with}$$

$$\widetilde{\boldsymbol{s}}^{\langle\ell\rangle} \equiv \begin{bmatrix} 1/E_1 & -\nu_{12}/E_1 & -\nu_{13}/E_1 & 0 & 0 & 0 \\ -\nu_{12}/E_1 & 1/E_2 & -\nu_{23}/E_2 & 0 & 0 & 0 \\ -\nu_{13}/E_1 & -\nu_{23}/E_2 & 1/E_3 & 0 & 0 & 0 \\ 0 & 0 & 0 & 1/G_{23} & 0 & 0 \\ 0 & 0 & 0 & 0 & 1/G_{13} & 0 \\ 0 & 0 & 0 & 0 & 0 & 1/G_{12} \end{bmatrix}^{\langle\ell\rangle} \tag{8}$$

where $\widetilde{\boldsymbol{s}}^{\langle\ell\rangle}$ is the compliance matrix of the ℓ-th lamina in the local material reference system, E_1, E_2, and E_3 are the Young's moduli, G_{23}, G_{13}, and G_{12} are the shear moduli, and ν_{23}, ν_{13}, and ν_{12} are the Poisson's ratios. The constitutive relationship given in Eq. (8) is then expressed in the global reference system using the transformation relationships for fourth-order tensor components, which lead to the constitutive behavior written as

$$\boldsymbol{\sigma}^{\langle\ell\rangle} = \boldsymbol{c}^{\langle\ell\rangle}\boldsymbol{\gamma}^{\langle\ell\rangle}, \tag{9}$$

where $\boldsymbol{c}^{\langle\ell\rangle} \equiv \mathbf{T}(\theta^{\langle\ell\rangle})\widetilde{\boldsymbol{c}}^{\langle\ell\rangle}\mathbf{T}^{\intercal}(\theta^{\langle\ell\rangle})$ and $\mathbf{T}(\theta^{\langle\ell\rangle})$ is a standard transformation matrix [41,42]. The constitutive relationship in Eq. (8) is employed for BT_n with $n \geq 2$; on the other hand, when $n = 1$, the constitutive coefficients are modified such that $\widetilde{s}^{\langle\ell\rangle}_{12} = \widetilde{s}^{\langle\ell\rangle}_{13} = \widetilde{s}^{\langle\ell\rangle}_{23} = \widetilde{s}^{\langle\ell\rangle}_{21} = \widetilde{s}^{\langle\ell\rangle}_{31} = \widetilde{s}^{\langle\ell\rangle}_{32} = 0$, and $\widetilde{s}^{\langle\ell\rangle}_{44} = 1/(\kappa_s G_{23})$ and $\widetilde{s}^{\langle\ell\rangle}_{55} = 1/(\kappa_s G_{13})$, where κ_s is the shear factor, assumed constant and equal to 5/6 in this paper.

On the other hand, in PTs, the wing is discretized using two-dimensional elements $\mathscr{D}^e$ mapping a portion of the span, a portion of the chord and the whole thickness of the wing, i.e., $\mathscr{D}^e \equiv [(e_1 - 1)h_1, e_1 h_1] \times [(e_2 - 1)h_2, e_2 h_2] \times [-\zeta/2, \zeta/2]$, where $e_1 = 1, \dots, n_1$, being n_1 the number of elements along the chord, $e_2 = 1, \dots, n_2$, being n_2 the number of elements along the span, $h_1 \equiv c/n_1$ and $h_2 \equiv 1/n_2$; in this case, the total number of element is $N_e = n_1 n_2$. In terms of kinematic behavior, the nth order PT is denoted by PT_n and corresponds to setting $p_3 = n$ in Eq. (5), while $p_1 = p_2 = p$ is varied independently and it is used to identify the order of the chosen DG_p formulation. In terms of constitutive behavior, wings represented by PT_n models with $n \geq 2$ feature the stress–strain relationship given in Eq. (8), whereas, when $n = 1$, the constitutive coefficients are modified such that $\widetilde{s}^{\langle\ell\rangle}_{13} = \widetilde{s}^{\langle\ell\rangle}_{23} = \widetilde{s}^{\langle\ell\rangle}_{31} = \widetilde{s}^{\langle\ell\rangle}_{32} = 0$, and $\widetilde{s}^{\langle\ell\rangle}_{44} = 1/(\kappa_s G_{23})$ and $\widetilde{s}^{\langle\ell\rangle}_{55} = 1/(\kappa_s G_{13})$, where $\kappa_s = 5/6$ is the same shear factor employed for BT_1 models.

3.1. Discontinuous Galerkin formulation

Once the kinematic approximation given in Eq. (5) or Eq. (6) is introduced for each structural element, the boundary conditions as well as the continuity of the solution between adjacent elements are enforced by employing an Interior Penalty discontinuous Galerkin formulation that has been recently developed for beam [36,43], plate [44,45] and shell [46–49] structures. In particular, each basis function $b^e(\xi_1, \xi_2, \xi_3)$ contained in the matrix $\boldsymbol{B}^e$ of Eq. (6) is taken from a space $\mathcal{V}^h$ of discontinuous polynomial fields defined as

$$\mathcal{V}^h \equiv \{b : \mathscr{D}^h \to \mathbb{R} \mid b(\boldsymbol{\xi} \in \mathscr{D}^e) \in \mathcal{P}^e_{p_1 p_2 p_3} \ \forall e = 1, \dots, N_e\}, \tag{10}$$

where $\mathscr{D}^h \equiv \bigcup_{e=1}^{N_e} \mathscr{D}^e$ denotes the collection of the mesh elements and $\mathcal{P}_{p_1 p_2 p_3}$ denotes the space of polynomials up to degree p_k in the variable ξ_k, with $k = 1, 2, 3$. Then, it is possible to show, see also Ref. [50], that the DG formulation for a small-strain linear-elastic problem is stated as follows: find $\boldsymbol{u}^h \in (\mathcal{V}^h)^{N_u}$ such that

$$B(\boldsymbol{v}, \boldsymbol{u}^h) = L(\boldsymbol{v}, \boldsymbol{f}, \boldsymbol{t}), \quad \forall \boldsymbol{v} \in (\mathcal{V}^h)^{N_u}, \tag{11}$$

where

$$\begin{aligned} B(\boldsymbol{v}, \boldsymbol{u}^h) \equiv & \int_{\mathscr{D}^h} \frac{\partial \boldsymbol{v}^{\intercal}}{\partial x_k} \boldsymbol{c}_{kl} \frac{\partial \boldsymbol{u}^h}{\partial x_l} \, \mathrm{d}V \\ & - \int_{\mathscr{F}^h} \left[[\![\boldsymbol{v}]\!]^{\intercal}_k \left\{ \boldsymbol{c}_{kl} \frac{\partial \boldsymbol{u}^h}{\partial x_l} \right\} + \left\{ \frac{\partial \boldsymbol{v}^{\intercal}}{\partial x_k} \boldsymbol{c}_{kl} \right\} [\![\boldsymbol{u}^h]\!]_l \right] \mathrm{d}S \\ & + \int_{\mathscr{F}^h} \mu [\![\boldsymbol{v}]\!]^{\intercal}_k [\![\boldsymbol{u}^h]\!]_k \, \mathrm{d}S + \\ & - \int_{\mathscr{B}^h_D} \left[n_k \boldsymbol{v}^{\intercal} \left(\boldsymbol{c}_{kl} \frac{\partial \boldsymbol{u}^h}{\partial x_l} \right) + \left(\frac{\partial \boldsymbol{v}^{\intercal}}{\partial x_k} \boldsymbol{c}_{kl} \right) \boldsymbol{u}^h n_l \right] \mathrm{d}S \\ & + \int_{\mathscr{B}^h_D} \mu \boldsymbol{v}^{\intercal} \boldsymbol{u}^h \, \mathrm{d}S \end{aligned} \tag{12}$$

and

$$L(\boldsymbol{v}, \boldsymbol{f}, \boldsymbol{t}) \equiv \int_{\mathscr{D}^h} \boldsymbol{v}^{\intercal} \boldsymbol{f} \, \mathrm{d}V + \int_{\mathscr{B}^h_N} \boldsymbol{v}^{\intercal} \boldsymbol{t} \, \mathrm{d}S. \tag{13}$$

In Eq. (12), the subscripts k and l span the set $\{1, 2, 3\}$ and imply summation when repeated, $\boldsymbol{c}_{kl}$ are 3×3 matrices that contain subsets of the elastic coefficients and are defined as $\boldsymbol{c}_{kl} \equiv \boldsymbol{I}^{\intercal}_k \boldsymbol{c} \boldsymbol{I}_l$, where $\boldsymbol{I}_k$ are 6×3 matrices containing ones and zeros only that can be found for instance in [45], n_k is the kth components of the unit normal vector at the element boundaries, μ is the penalty parameter typical of Interior Penalty DG formulations, and the terms $\{\bullet\}$ and $[\![\bullet]\!]_k$ represent the average and the jump operators, respectively, defined at the interface i between two contiguous elements e and e' as

$$\{\bullet\}^i \equiv \frac{1}{2}\left(\bullet^e + \bullet^{e'}\right) \quad \text{and} \quad [\![\bullet]\!]^i_k \equiv \bullet^e n^e_k + \bullet^{e'} n^{e'}_k. \tag{14}$$

Additionally, the integrals appearing in Eqs. (12) and (13) are typically referred to as the broken integrals and are defined as

$$\begin{aligned} & \int_{\mathscr{D}^h} \bullet \, \mathrm{d}V \equiv \sum_{e=1}^{N_e} \int_{\mathscr{D}^e} \bullet^e \, \mathrm{d}V, \quad \int_{\mathscr{B}^h_D} \bullet \, \mathrm{d}S \equiv \sum_{e=1}^{N_e} \int_{\mathscr{B}^e_D} \bullet^e \, \mathrm{d}S, \\ & \int_{\mathscr{B}^h_N} \bullet \, \mathrm{d}S \equiv \sum_{e=1}^{N_e} \int_{\mathscr{B}^e_N} \bullet^e \, \mathrm{d}S, \quad \text{and} \quad \int_{\mathscr{F}^h} \bullet \, \mathrm{d}S \equiv \sum_{i=1}^{N_i} \int_{\mathscr{F}^i} \bullet^i \, \mathrm{d}S, \end{aligned} \tag{15}$$

where $\mathscr{B}_D^e$ and $\mathscr{B}_N^e$ are the portions of the eth element's boundary where Dirichlet boundary conditions and Neumann boundary conditions, respectively, are enforced, while $\mathscr{I}^i$ is a generic interface between two contiguous elements and $\mathscr{I}^h \equiv \bigcup_{i=1}^{N_i} \mathscr{I}^i$ denotes the collection of all the inter-element interfaces associated with the considered mesh. It is worth noting that volume and boundary integrals spanning the thickness of the wing are computed accounting for the multilayered structure of the wing and the constitutive behavior of each lamina; in particular, on the basis of the order n of the considered beam or plate theory, a suitable number of quadrature points are considered throughout the thickness of each lamina and the matrices $\boldsymbol{c}_{kl}$ are computed using the stiffness matrix $\boldsymbol{c}^{\langle \ell \rangle}$ when the generic quadrature point falls within the ℓ-th lamina.

Eventually, by letting $\boldsymbol{v}$ span all the basis functions contained in $(\mathcal{V}^h)^{N_u}$, the following algebraic system of equations is obtained

$$\mathbf{K}_{\mathsf{S}}\mathbf{X}_{\mathsf{S}} = \mathbf{F}, \tag{16}$$

where $\mathbf{K}_{\mathsf{S}}$ and $\mathbf{F}$ are the stiffness matrix and the right-hand side stemming from the terms $B(\boldsymbol{v},\boldsymbol{u}^h)$ and $L(\boldsymbol{v},\boldsymbol{f},t)$, respectively, in Eq. (11), and $\mathbf{X}_{\mathsf{S}}$ is the vector containing the unknown structural degrees of freedom associated with the considered structural theory and DG formulation. It is worth noting that the total number of degrees of freedom (DOF) associated with the structural model is given by $\mathsf{DOF} = N_e N_u N_p$. Additionally, for the sake of completeness, the explicit expression of the elemental contributions to the stiffness matrix within the considered Interior Penalty DG formulation is reported in Appendix A.

4. Aerodynamic model

As anticipated above, the vortex lattice method [51] is employed as aerodynamic model to be coupled with the DG structural model for static aeroelastic analysis. The method is briefly recalled in this section for self-completeness; however interested readers are referred to Ref. [51] for further details.

In the formulation a set of bound ring and horseshoe vortexes is associated with the wing mean surface, forming the well-known vortex lattice. Each vortex i features a strength Γ^i, initially unknown, and contributes to generate a spatial flow velocity field that can be computed through the standard Biot–Savart law. The superposition of the free-stream speed $\boldsymbol{V}_\infty$ and the velocity induced by the collection of all vortexes generates a resulting flow field $\boldsymbol{v}$ that, at a generic point $\boldsymbol{x}$, can be expressed as

$$\boldsymbol{v}(\boldsymbol{x}) = \boldsymbol{V}_\infty + \sum_{i=1}^{N_v} \boldsymbol{v}^i(\boldsymbol{x})\Gamma^i, \tag{17}$$

where $\boldsymbol{v}^i(\boldsymbol{x})$ is the velocity induced by the i-th vortex with unit strength and N_v is the total number of vortexes. To determine the vortex strengths, the aerodynamic flow impenetrability condition $\boldsymbol{v}(\boldsymbol{x}_c^i)\cdot\hat{\boldsymbol{n}}^i = 0$ must be enforced at the vortexes control points, where $\boldsymbol{x}_c^i$ collects the coordinates of the ith vortex control point and $\hat{\boldsymbol{n}}^i$ is the unit normal to the wing mean surface at $\boldsymbol{x}_c^i$, see Fig. 2. By letting i cycle over all the vortexes, the linear system

$$\mathbf{A}\,\boldsymbol{\Gamma} = \mathbf{b} \tag{18}$$

is assembled, where the ij-th term A_{ij} of the coefficient matrix $\mathbf{A}$ is given by $A_{ij} \equiv \hat{\boldsymbol{n}}^i \cdot \boldsymbol{v}^j$, the ith term b_i of the right-hand side $\mathbf{b}$ is given by $b_i \equiv -\hat{\boldsymbol{n}}^i \cdot \boldsymbol{V}_\infty$, and $\boldsymbol{\Gamma}$ is the vector containing the unknown strengths associated with the considered lattice of vortexes.

Upon resolution of the aerodynamic field, the aerodynamic force $\boldsymbol{f}^i$ acting on the ith vortex can be computed as

$$\boldsymbol{f}^i = \rho_\infty \boldsymbol{v}(\boldsymbol{x}_m^i) \times \boldsymbol{l}^i \widetilde{\Gamma}^i, \tag{19}$$

where ρ_∞ is the density of the flow, $\boldsymbol{l}^i$ is the vector associated with leading segment of the ring/horseshoe vortex, $\boldsymbol{v}(\boldsymbol{x}_m^i)$ is the local flow velocity evaluated at the midpoint $\boldsymbol{x}_m^i$ of $\boldsymbol{l}^i$, and $\widetilde{\Gamma}^i$ is the net circulation strength at the leading segment of the vortex, coinciding with Γ^i if the ith vortex is at the leading edge of the wing, or otherwise with the difference between the circulation values of two adjacent vortexes along the chord direction. As an example, considering Fig. 2(b), the force generated by the vortex i is given by $\boldsymbol{f}^i = \rho_\infty \boldsymbol{v}(\boldsymbol{x}_m^i)\times \boldsymbol{l}^i \Gamma^i$, whereas the force generated by the vortex j is given by $\boldsymbol{f}^j = \rho_\infty \boldsymbol{v}(\boldsymbol{x}_m^j)\times \boldsymbol{l}^j (\Gamma^j - \Gamma^i)$.

5. Aeroelastic coupling

The discrete equations governing the structural and aerodynamic problems are represented by Eqs. (16) and (18), respectively. These equations are mutually coupled: the forces generated by the vortex lattice enter the right-hand side of Eq. (16) via the body force term appearing in Eq. (13) as a set of concentrated forces, i.e., $\boldsymbol{f} = \sum_{i=1}^{N_v} \boldsymbol{f}^i \delta(\boldsymbol{x} - \boldsymbol{x}_m^i)$, where $\delta(\boldsymbol{x}-\boldsymbol{x}^i)$ is the Dirac delta function at the point $\boldsymbol{x}^i$. On the other hand, both the coefficient matrix $\mathbf{A}$ and the right-hand side vector $\mathbf{b}$ of Eq. (18) are computed using the unit normal to the wing's mean surface, which is affected by the deformation of the structure. As a consequence, assuming that the wing will be subject to aerodynamic loads only, the two systems of equations can be re-written by explicitly expressing the dependence of each term on the structural unknowns $\mathbf{X}_{\mathsf{S}}$ and aerodynamic unknowns $\boldsymbol{\Gamma}$ as

$$\begin{cases} \mathbf{A}(\mathbf{X}_{\mathsf{S}})\boldsymbol{\Gamma} = \mathbf{b}(\mathbf{X}_{\mathsf{S}}) \\ \mathbf{K}_{\mathsf{S}}\mathbf{X}_{\mathsf{S}} = \mathbf{F}(\boldsymbol{\Gamma}), \end{cases} \tag{20}$$

which represents a non-linear system of equations that may be solved via a root-searching technique, such as the Newton–Raphson method. However, assuming small perturbations, another solution approach consists in linearizing Eq. (20) with respect to the reference undeformed non-lifting configuration.

Using the subscript 0 to denote quantities computed for $\mathbf{X}_{\mathsf{S}} = \mathbf{0}$ and $\boldsymbol{\Gamma} = \mathbf{0}$, the linearization is performed as follows: the aerodynamic coefficient matrix is replaced by the matrix $\mathbf{A}_0$, i.e., $\mathbf{A}(\mathbf{X}_{\mathsf{S}}) \approx \mathbf{A}_0 \equiv \mathbf{A}(\mathbf{X}_{\mathsf{S}} = \mathbf{0})$. The aerodynamic right-hand side is replaced by its first-order Taylor expansion with respect to the structural degrees of freedom, i.e.,

$$\mathbf{b}(\mathbf{X}_{\mathsf{S}}) \approx \mathbf{b}_0 + \left.\frac{\partial \mathbf{b}}{\partial \mathbf{X}_{\mathsf{S}}}\right|_0 \mathbf{X}_{\mathsf{S}}, \tag{21}$$

where $\mathbf{b}_0 \equiv \mathbf{b}(\mathbf{X}_{\mathsf{S}} = \mathbf{0})$ is obtained by considered the unit normal to the lifting surface in the undeformed configuration, while the explicit expression of the entries of the matrix $\partial\mathbf{b}/\partial\mathbf{X}_{\mathsf{S}}|_0$ is provided in Appendix B. It is worth noting that, in other similar approaches, such as those implemented in NASTRAN or in the literature, see e.g. Ref. [29], the coupling of the structural and the aerodynamic fields is performed via a spline method, which allows reconstructing the displacement field at points that are not the nodes of the structural mesh; here such spline methods are not needed.

Moreover, the structural right-hand side is expressed as a first-order Taylor expansion with respect to the aerodynamic degrees of freedom as

$$\mathbf{F}(\boldsymbol{\Gamma}) \approx \left.\frac{\partial \mathbf{F}}{\partial \boldsymbol{\Gamma}}\right|_0 \boldsymbol{\Gamma}, \tag{22}$$

where, also in this case, the entries of the matrix $\partial\mathbf{F}/\partial\boldsymbol{\Gamma}|_0$ are explicitly given in Appendix B.

Based on the hypotheses discussed above, Eq. (20) can be rewritten as

$$\begin{cases} \mathbf{A}_0\boldsymbol{\Gamma} = \mathbf{b}_0 + \left.\frac{\partial \mathbf{b}}{\partial \mathbf{X}_{\mathsf{S}}}\right|_0 \mathbf{X}_{\mathsf{S}} \\ \mathbf{K}_{\mathsf{S}}\mathbf{X}_{\mathsf{S}} = \left.\frac{\partial \mathbf{F}}{\partial \boldsymbol{\Gamma}}\right|_0 \boldsymbol{\Gamma}, \end{cases} \tag{23}$$

leading, after a few algebraic manipulations, to the following linear system of equations

$$\mathbf{K}_{\mathsf{AE}}\mathbf{X}_{\mathsf{S}} = \mathbf{F}_{\mathsf{AE}}, \tag{24}$$

where the aeroelastic stiffness matrix $\mathbf{K}_{\mathsf{AE}}$ and the aeroelastic right-hand side $\mathbf{F}_{\mathsf{AE}}$ are given as

$$\mathbf{K}_{\mathsf{AE}} \equiv \mathbf{K}_{\mathsf{S}} - \left.\frac{\partial \mathbf{F}}{\partial \boldsymbol{\Gamma}}\right|_0 \mathbf{A}_0^{-1} \left.\frac{\partial \mathbf{b}}{\partial \mathbf{X}_{\mathsf{S}}}\right|_0 \quad \text{and} \quad \mathbf{F}_{\mathsf{AE}} \equiv \left.\frac{\partial \mathbf{F}}{\partial \boldsymbol{\Gamma}}\right|_0 \mathbf{A}_0^{-1}\mathbf{b}_0. \tag{25}$$

In this work the aeroelastic response of the considered composite multi-layer wings is computed employing Eqs. (23)–(25), while more general cases will be considered in future investigations, as discussed in Section 7.

Eventually, the linear aeroelastic problem given in Eq. (24) allows performing a stability analysis and computing the divergence speed V_D for the considered wing by solving the associated eigenvalue problem

$$\left(\mathbf{K}_S - \rho_\infty V_D^2 \hat{\mathbf{K}}_A\right)\mathbf{X}_S = \mathbf{0}, \tag{26}$$

where the matrix $\hat{\mathbf{K}}_A$ is obtained by considering unit density and unit free-stream velocity in the evaluation of the terms **F** and **b** of Eq. (23), i.e.

$$\hat{\mathbf{K}}_A \equiv \left(\left.\frac{\partial \mathbf{F}}{\partial \boldsymbol{\Gamma}}\right|_0 \mathbf{A}_0^{-1} \left.\frac{\partial \mathbf{b}}{\partial \mathbf{X}_S}\right|_0 \right)_{\rho_\infty=1, V_\infty=1}. \tag{27}$$

6. Numerical results

This section reports the results of the computational tests performed using the proposed DG-VLM aeroelastic method. The convergence and accuracy of the results have been assessed considering both the aeroelastic *response* and the *static instability* conditions. The aeroelastic response has been expressed in terms of wing tip deflection $u_z|_{\text{tip}}$, computed at the leading edge of the wing tip chord, and wing tip twist $\Delta u_z|_{\text{tip}} \equiv u_z|_{\text{LE}} - u_z|_{\text{TE}}$, while the static instability conditions is described in terms of divergence speed V_D. Both single-layer and multi-layer wing plates have been analyzed, considering the effects of free-stream velocity V_∞, wing aspect ratio, sweep angle Λ, material properties and stacking sequence. Different single-ply properties have been considered, as summarized in Table 1. Both beam theories – BT_n – and plate theories – PT_n – have been tested for different DG_p schemes, where it is recalled that the subscript n refers to the order of the polynomial expansion of the kinematics over the transverse section of the beam or along the thickness of the plate, while the subscript p identifies the order of expansion of the kinematics along the beam span or over the plate plane.

All the DG computations have been performed using PySCo,[1] a python in-house framework for scientific computing that also implements the developed aeroelastic method. On the other hand, the reference FE solutions have been computed employing shell elements with the NASTRAN SOL 144 aeroelastic module. Also, when DG and FE solutions are compared, the same aerodynamic grid has been employed, although DG is coupled with VLM while FEs are coupled with the doublet lattice method (DLM) within NASTRAN.

6.1. Static aeroelastic analysis of a single-layer wing plate

First, the formulation has been validated for single-layer wing plates.

In the first set of tests, a single-layer wing with rectangular planform, no sweep, i.e. $\Lambda = 0°$, constant chord $c = 1\,\text{m}$, half span $b/2 = 2\,\text{m}$ and thickness ratio $\zeta/c = 0.01$ is considered. It is worth noting that such a thickness ratio is employed for numerical purposes only. The material properties are those of *Material 1* in Table 1, and the layer is oriented so that the material reference direction 1 is aligned with the axis x_2, normal to the free-stream direction. The steady aerodynamic flow features an angle of attack $\alpha = 1°$ and the aeroelastic response is evaluated at $V_\infty = 30\,\text{m/s}$; in all the performed tests the aeroelastic response has been computed considering $V_\infty \approx V_D/2$, so to retrieve meaningful but not excessive deflections.

Fig. 3 reports the convergence analysis for the wing aeroelastic response and static divergence speed. The reference FE solution has been computed using shell elements within the NASTRAN aeroelastic module. The BT_1 and PT_1 DG theories assume plane stress and employ shear correction factors, see Section 3. The same 10×50 aerodynamic grid has been used with both DG and FE solutions. The dark and light gray areas in the plots identify regions whose error $\Delta\epsilon$ with respect to the NASTRAN converged value $\bar{q}$ of the considered quantity q lies within $\Delta\epsilon = \pm 1\%$ and $\Delta\epsilon = \pm 5\%$.

It is observed that, for this case, both beam and plate theories exhibit fully satisfying convergence to the converged finite element (FE) solutions, both in terms of tip deflection $u_z|_{\text{tip}}$ (computed at leading edge) and tip twist $\Delta u_z|_{\text{tip}}$, as well as in terms of divergence speed V_D. Indeed only the lowest order beam theory BT_1 converges to a value of $u_z|_{\text{tip}}$ at the margin of the dark gray area for all orders of span-wise expansion p of the underlying DG_p scheme, which signals a 1% difference with respect the reference FE solution only for the less slender wing. No other remarkable differences between beam and plate theories are observed for this case study and also the order of expansion n along the transverse dimension has limited effect on the convergence values and convergence speed with respect to the number of DOF. On the contrary, a marked effect on the convergence speed is exerted by the order of expansion p, as it can be observed form the curves corresponding to $p \geq 4$. In particular, it is observed that while FEs converge faster than the proposed scheme in terms of tip deflection $u_z|_{\text{tip}}$, faster convergence of DG_p with respect to FEs is generally obtained when $p \geq 4$ both in terms of wing tip twist $\Delta u_z|_{\text{tip}}$ and divergence speed V_D, for both beam and plate theories.

Possible effects of the aspect ratio on the numerical convergence of the computational scheme are investigated performing an analogous analysis on a wing with longer half-span $b/2 = 4\,\text{m}$, while the other material and geometric features are kept the same as those in the previous set of tests. The wing aeroelastic response is computed for $V_\infty = 10\,\text{m/s}$.

Fig. 4 shows how, for the higher aspect ratio considered, no relevant differences between beam and plate theories are detected, neither when the lowest order beam theory is adopted, which confirms how beam models may be preferable for analyzing high aspect ratio wings. The same considerations as those reported above about the effects of the selected transverse and span-wise orders of polynomial expansions can be reported for this case, confirming the higher relevance of the order of expansion p of the underlying DG_p scheme on its convergence features. Regarding the comparison with the reference FE solution: (*i*) faster convergence with respect to the number of DOF of the FE solution is observed for the wing tip deflection $u_z|_{\text{tip}}$; (*ii*) a slightly faster convergence of the DG scheme is revealed for the wing tip twist $\Delta u_z|_{\text{tip}}$; (*iii*) comparable convergence speed is observed for the divergence speed computation.

Eventually, the accuracy of the proposed scheme for single-layer wing plates has been assessed considering the effect of the material lamination angle θ on the wing static aeroelastic response and the combined effects of θ and the sweep angle Λ on the wing static divergence. For the definitions of θ and Λ see Fig. 1.

Fig. 5 reports both the wing tip deflection $u_z|_{\text{tip}}$ and twist $\Delta u_z|_{\text{tip}}$ versus the lamination angle θ for a rectangular wing with no sweep $\Lambda = 0°$, constant chord $c = 1\,\text{m}$, half-span $b/2 = 10\,\text{m}$ and $\zeta/c = 0.1$, subject to a free-stream flow with $\alpha = 1°$ and $V_\infty = 50\,\text{m/s}$. Also in this case, the considered thickness ratio is employed for numerical purposes only. The DG solution is computed using 2×5 plate elements over the

Table 1
Single-ply orthotropic material properties considered in the performed aeroelastic analyses.

Property	Symbol	Mat.1	Mat.2	Mat.3	Unit
Longitudinal Modulus	E_1	20.5	98.0	181.0	GPa
Transverse Moduli	E_2, E_3	10.0	7.9	10.27	GPa
Shear Moduli	G_{23}, G_{13}, G_{12}	5.0	5.6	7.17	GPa
Poisson ratios	ν_{23}, ν_{13}, ν_{12}	0.25	0.28	0.28	

[1] https://gitlab.com/aeropa/pysco

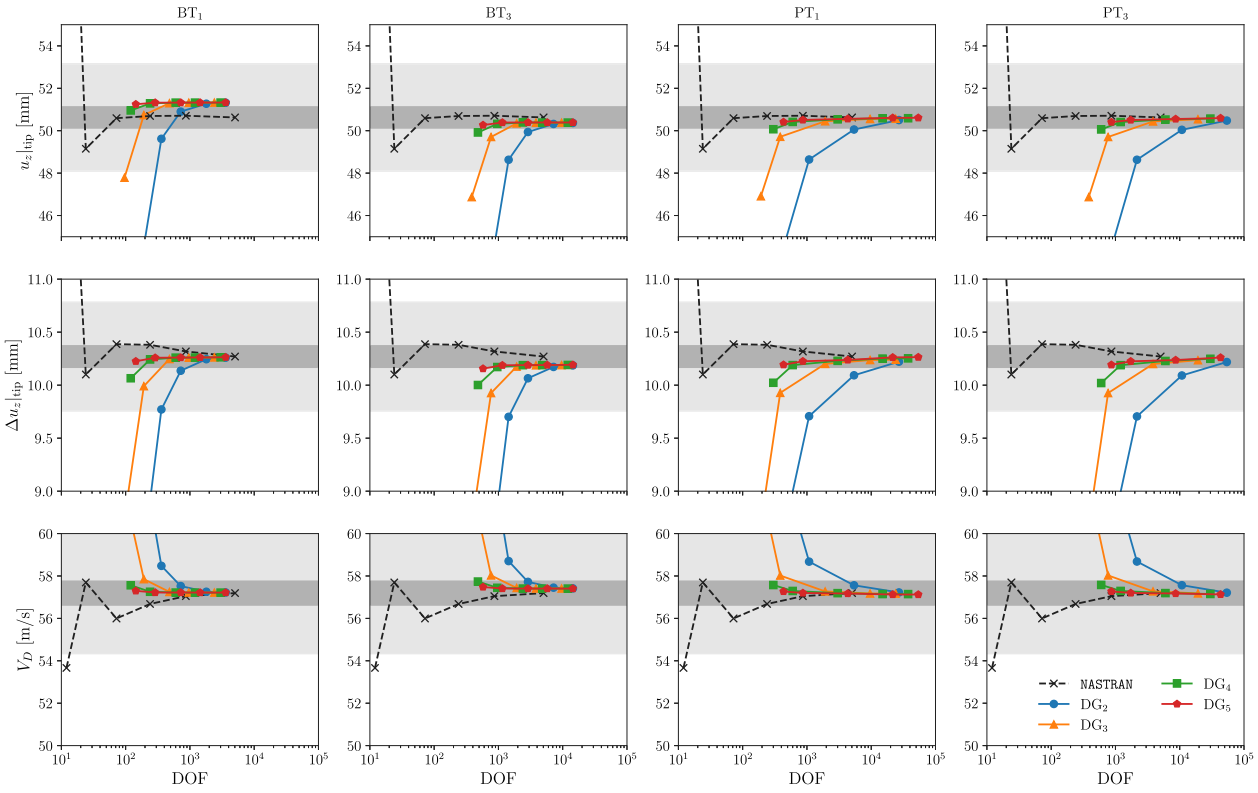

Fig. 3. Convergence of the computed aeroelastic response and divergence speed V_D with respect to the number of DOF for a single-layer wing subject to steady aerodynamic flow. Wing features: rectangular planform, chord $c = 1\,\text{m}$, half-span $b/2 = 2\,\text{m}$, $\zeta/c = 0.01$, $\Lambda = 0°$, see Fig. 1 for reference. Wing material: *Material* 1, see Table 1, single-layer, lamination angle $\theta = 90°$ (fibers aligned with the x_2 global axis). Aerodynamic flow: steady flow, $\alpha = 1°$; aeroelastic response evaluated at $V_\infty = 30\,\text{m/s}$.

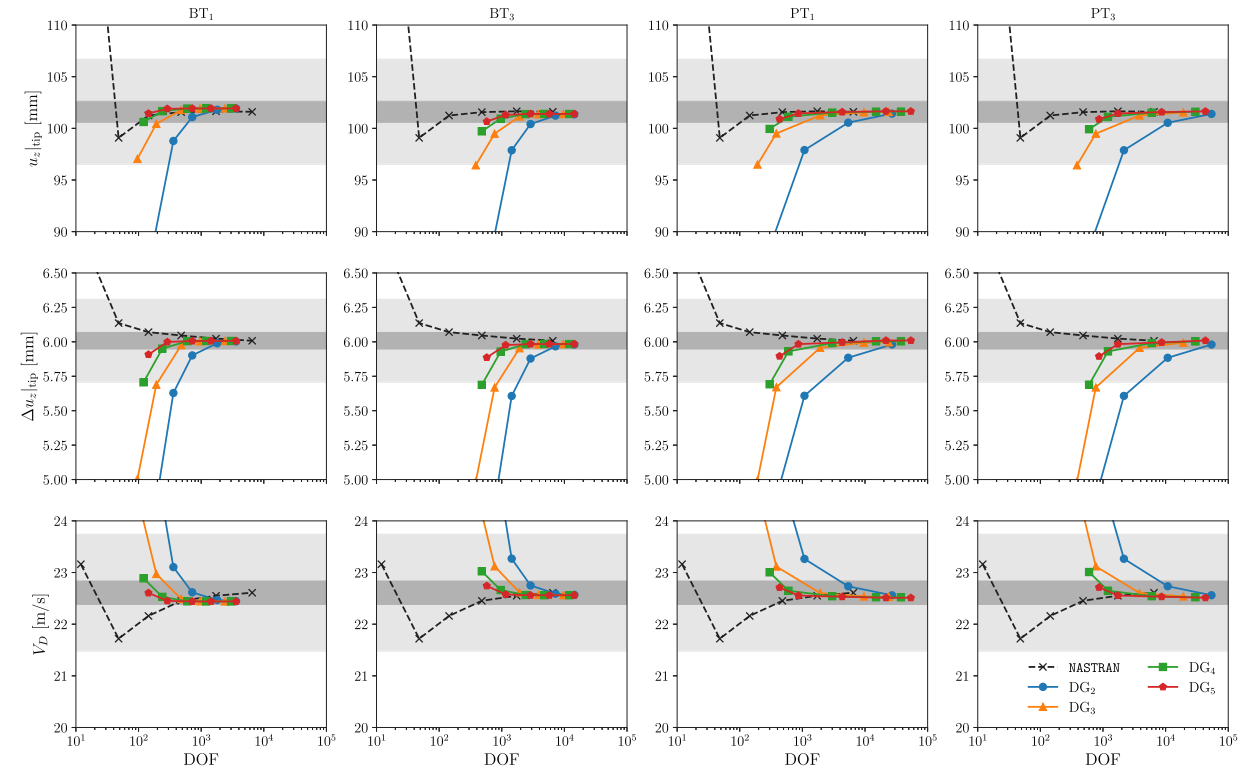

Fig. 4. Convergence of the computed aeroelastic response and divergence speed V_D with respect to the number of DOF for a single-layer wing subject to steady aerodynamic flow. Wing features: rectangular planform, chord $c = 1\,\text{m}$, half-span $b/2 = 4\,\text{m}$, $\zeta/c = 0.01$, $\Lambda = 0°$, see Fig. 1 for reference. Wing material: *Material* 1, see Table 1, single-layer, lamination angle $\theta = 90°$ (fibers aligned with the x_2 global axis). Aerodynamic flow: steady flow, $\alpha = 1°$; aeroelastic response evaluated at $V_\infty = 10\,\text{m/s}$.

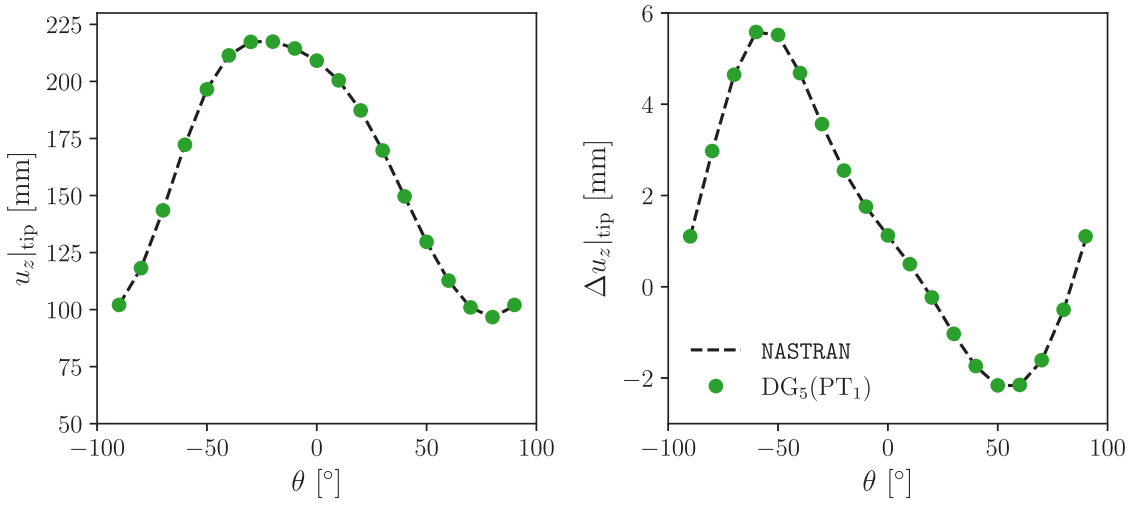

Fig. 5. Wing tip deflection $u_z|_{\text{tip}}$ and twist $\Delta u_z|_{\text{tip}}$ of a single-layer composite wing plate as a function of the lamination angle θ. Wing features: rectangular planform, $\Lambda = 0°$, $c = 1\,\text{m}$, $b/2 = 10\,\text{m}$, $\zeta/c = 0.1$, single-layer, *Material* 1 (see Table 1). Aerodynamic flow: $\alpha = 1°$, $V_\infty = 50\,\text{m/s}$.

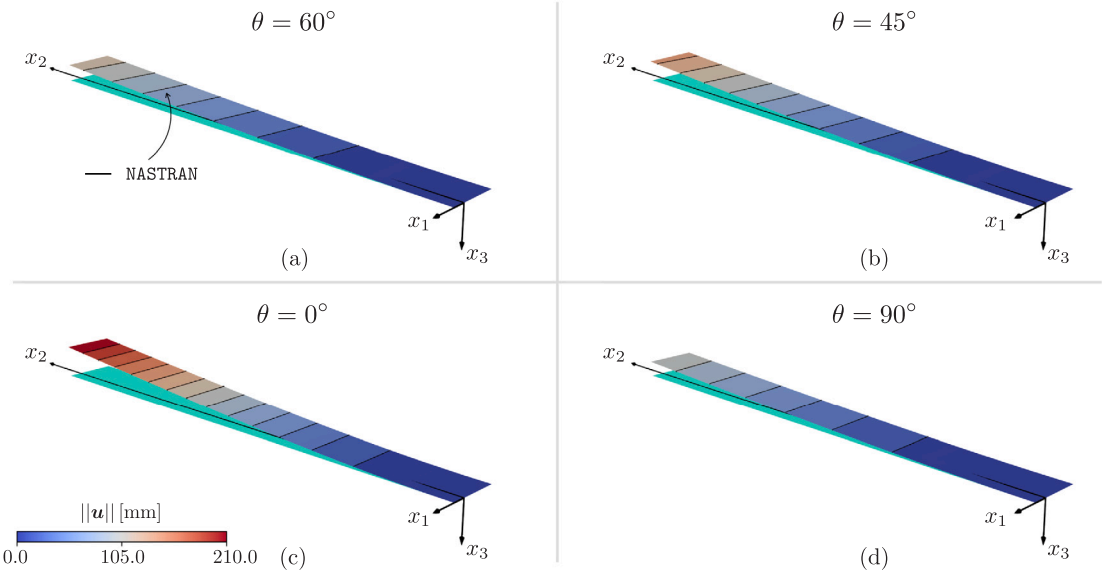

Fig. 6. Deformed configuration of a single-layer orthotropic wing plate for the four values of the lamination angle $\theta = \{60°, 45°, 0°, 90°\}$. Wing features: $\Lambda = 0°$, $c = 1\,\text{m}$, $b/2 = 10\,\text{m}$, $\zeta/c = 0.1$, single-layer, *Material* 1 (see Table 1). Flow features: $\alpha = 1°$, $V_\infty = 50\,\text{m/s}$. The color-graded plots correspond to the solution computed using the proposed DG scheme; the black continuous lines represent the solution provided by FE NASTRAN analysis.

wing reference plane, with polynomial expansion of order $(p_1, p_2, p_3) = (5, 5, 1)$ over each element – see Eq. (5) – which corresponds to the DG_5 PT_1 theory featuring 216 DOF per element and 2160 DOF for the whole structure. The reference NASTRAN solution has been computed employing a structured mesh of 10 × 100 shell elements. The same 10 × 50 aerodynamic grid has been used for both the proposed and benchmark methods. The two solutions match perfectly over the whole range of θ. It is also observed how the lamination angle plays an important role for the aeroelastic response, as it is possible to identify specific angles that minimize the wing tip deflection/twist in given free-stream conditions.

Fig. 6 shows the deformed configuration of the wing considered above – $\Lambda = 0°$, $c = 1\,\text{m}$, $b/2 = 10\,\text{m}$, $\zeta/c = 0.1$, $\alpha = 1°$ and $V_\infty = 50\,\text{m/s}$ – for the four different values of the lamination angle $\theta = \{60°, 45°, 0°, 90°\}$. The color-plot of the deformed wing plate mid-plane, obtained from the DG solution, is superimposed on the FE solution computed with NASTRAN, sketched in black continuous lines, and a fully satisfying match is observed.

The analysis reported in Fig. 7 explores the combined effect of sweep and lamination angles, Λ and θ in Fig. 1, on the divergence speed V_D. Each curve corresponds to a selected sweep angle $\Lambda = \{0°, -10°, -20°\}$ and plots the divergence speed V_D as a function of the lamination angle $-90° \leq \theta \leq 0°$. The DG solution is computed adopting 2 × 5 (5 along the wing span) DG_5 PT_1 plate elements and it is compared with the FE results obtained using 10 × 100 shell elements within NASTRAN. Perfect match between the proposed and the benchmark solution is recorded for all the considered combinations of sweep and lamination angles. From a physical point of view it is observed as the lamination angle represents an important parameter in the context of aeroelastic tailoring, and how its interplay with other configuration choices must be carefully considered, as it may have a remarkable effect of the stability behavior of the lifting surfaces: in the present case, as well known from the literature, sweeping the wing forward has a tremendous effect on the divergence speed, for example reducing its value to less than half the value associated with the no-sweep configuration when $\theta = 0°$.

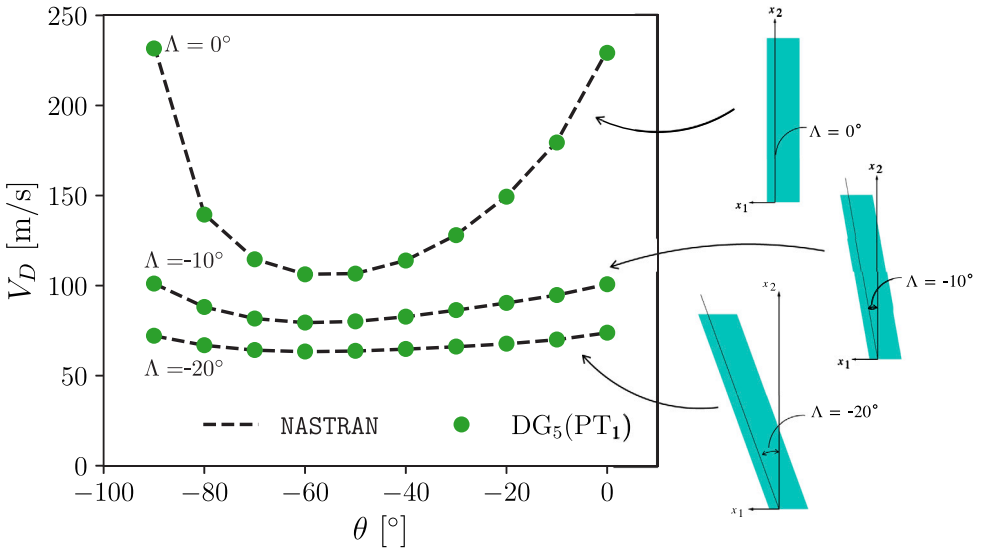

Fig. 7. Divergence speed V_D of a single-layer composite wing plate as a function of the lamination angle θ for different values of the sweep angle Λ. Wing features: rectangular planform, $c = 1\,\text{m}$, $b/2 = 10\,\text{m}$, $\zeta/c = 0.1$, single-layer, *Material 1* (Table 1). Aerodynamic flow: $\alpha = 1°$.

6.2. Static aeroelastic analysis of a multi-layer wing plate

Upon validating its accuracy for single-layer analysis, the proposed formulation has been tested for the analysis of multi-layer wing plates.

First, the static aeroelastic response and divergence speed of composite laminate wing plates with different stacking sequences have been computed. A multi-layer wing with rectangular planform, $\Lambda = 0°$, chord $c = 76.2\,\text{mm}$, half-span $b/2 = 305\,\text{mm}$, and overall thickness $\zeta = 0.804\,\text{mm}$ subject to a steady aerodynamic flow with $\alpha = 1°$ is considered; the aeroelastic response is computed for $V_\infty = 10\,\text{m/s}$. The orthotropic properties of the individual plies considered in this set of analyses are those of *Material 2* in Table 1.

Tables 2–4 report the results for flat composite laminate wing plates with stacking sequences $[90_2, 0]_S$, $[-45_2, 90]_S$, and $[-60_2, 90]_S$ respectively. The aeroelastic response is again expressed in terms of wing tip deflection $u_z|_{\text{tip}}$ and wing tip twist $\Delta u_z|_{\text{tip}}$, while the instability condition is identified in terms of divergence speed V_D. The DG solution has been computed employing either beam – BT$_n$ – or plate – PT$_n$ – theories, with $n = 1, 3$, and with different orders of polynomial expansion $p = 2, \ldots, 5$ of the underlying DG$_p$ formulation; 10 beam elements along the span have been employed for the beam theories, while 5×10 in-plane plate elements have been used for the plate theories. The reference FE solution has been obtained with 8×31 shell elements within NASTRAN. The aerodynamic grid consists of 10×50 panels, both in the proposed formulation and in the NASTRAN solver. The results reported in Tables 2–4 reveal that the solution provided by the proposed DG scheme always matches well with that provided by NASTRAN; on the other hand, some discrepancies with respect to some of the other numerical or experimental data available in the literature are observed for some of the analyzed test cases, probably to be attributed to different structural/aerodynamic assumptions. Overall, the obtained results are considered satisfactory and validate the method for the static aeroelastic analysis of multi-layer configurations.

Eventually, the combined effects of stacking sequence and sweep angle on the aeroelastic behavior of composite laminated wing plates are explored. Fig. 8 plots the aeroelastic response in terms of wing tip deflection $u_z|_{\text{tip}}$ and twist $\Delta u_z|_{\text{tip}}$ versus sweep angle Λ for different stacking sequences. The wing features $c = 1\,\text{m}$, $b/2 = 4\,\text{m}$, thickness ratio $\zeta/c = 0.01$ and it is subject to a steady aerodynamic flow with angle of attack $\alpha = 1°$; the aeroelastic response is computed for $V_\infty = 10\,\text{m/s}$. Two different stacking sequences are considered, namely $[0_2^\circ, 90_2^\circ]_S$ and $[0°, -45°, 45°, 90°]_S$, with the properties of the individual plies corresponding to those of *Material 3* in Table 1. The response computed by using the proposed method, specifically 2×4 DG$_5$ PT$_1$ plate elements leading to 1728 total structural DOF, is compared with the FE solution obtained by using 10×40 shell elements within the NASTRAN aeroelastic module. In both cases, the same 10×40 aerodynamic grid has been employed. From the computational point of view, it is highlighted how the DG solution perfectly matches the FE solution, thus confirming the accuracy and robustness of the proposed method. From the mechanical point of view, the considered results confirm the importance of the wing configuration and material architecture in determining the aeroelastic response: for a given sweep angle Λ, the selection of a certain stacking sequence may reduce or exacerbate the aeroelastic response. Accordingly, the potentially problematic aeroelastic behavior of swept forward wings can be addressed by selecting an appropriate stacking sequence and thus attenuating both wing deflection and twist.

Fig. 9 shows the deformed configuration of the same multi-layer wing plates, subject to the same aerodynamic free-stream conditions,

Table 2
Static aeroelastic response and divergence speed for a composite $[90_2, 0]_S$ laminate wing plate. Wing geometry: rectangular planform; $\Lambda = 0°$; $c = 76.2\,\text{mm}$; $b/2 = 305\,\text{mm}$; overall thickness $\zeta = 0.804\,\text{mm}$. Ply material properties: *Material 2* in Table 1. Aerodynamic flow: $\alpha = 1°$; aeroelastic response computed for $V_\infty = 10\,\text{m/s}$.

Theory	p	u_z [mm]	Δu_z [mm]	V_D [m/s]	DOF
BT$_1$	2	1.391	0.2694	28.77	360
	3	1.398	0.2713	28.66	480
	4	1.398	0.2713	28.66	600
	5	1.398	0.2713	28.66	720
BT$_3$	2	1.386	0.2694	28.75	1440
	3	1.392	0.2713	28.64	1920
	4	1.392	0.2713	28.64	2400
	5	1.392	0.2713	28.64	2880
PT$_1$	2	1.386	0.2696	28.73	2700
	3	1.393	0.2717	28.60	4800
	4	1.393	0.2720	28.59	7500
	5	1.394	0.2722	28.58	10800
PT$_3$	2	1.386	0.2696	28.73	5400
	3	1.393	0.2717	28.60	9600
	4	1.393	0.2720	28.59	15000
	5	1.394	0.2722	28.58	21600
NASTRAN		1.397	0.2723	28.57	1728
Ref. [52]		——	——	30.60	510
Ref. [53]		——	——	25.00	——

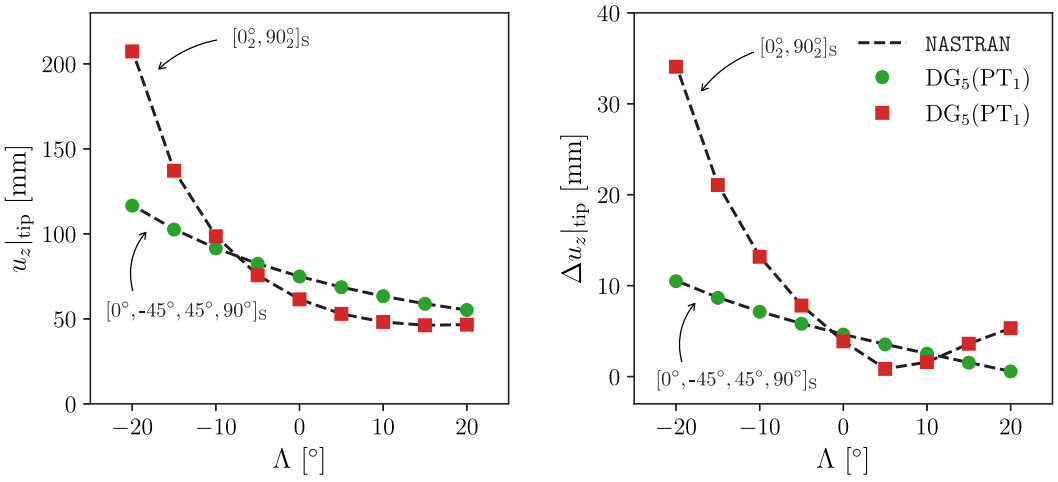

Fig. 8. Wing tip deflection $u_z|_{tip}$ and twist $\Delta u_z|_{tip}$ of multi-layer composite wing plates as a function of the sweep angle Λ and stacking sequence. Wing geometry: $c = 1$ m, $b/2 = 4$ m, $\zeta/c = 0.01$. Aerodynamic flow: $\alpha = 1°$, $V_\infty = 10$ m/s. DG solution: (2×4) DG_5 PT_1 plate elements. FE solution: NASTRAN, 10×40 shell elements. Aerodynamic grid: 10×40 elements for both the structural methods (DG is coupled with VLM, FEM is coupled with DLM).

Table 3
Static aeroelastic response and divergence speed for a composite $[-45_2, 90]_S$ laminate wing plate. Wing geometry: rectangular planform; $\Lambda = 0°$; $c = 76.2$ mm; $b/2 = 305$ mm; overall thickness $\zeta = 0.804$ mm. Ply material properties: *Material 2* in Table 1. Aerodynamic flow: $\alpha = 1°$; aeroelastic response computed for $V_\infty = 10$ m/s.

Theory	p	u_z [mm]	Δu_z [mm]	V_D [m/s]	DOF
BT_1	2	13.62	1.808	13.76	360
	3	14.56	1.941	13.51	480
	4	14.60	1.947	13.50	600
	5	14.60	1.947	13.50	720
BT_3	2	14.01	1.962	13.52	1440
	3	15.06	2.113	13.27	1920
	4	15.11	2.122	13.26	2400
	5	15.12	2.123	13.26	2880
PT_1	2	13.99	1.944	13.55	2700
	3	15.04	2.089	13.31	4800
	4	15.13	2.102	13.29	7500
	5	15.15	2.106	13.28	10800
PT_3	2	13.98	1.943	13.55	5400
	3	15.03	2.088	13.31	9600
	4	15.12	2.101	13.29	15000
	5	15.15	2.105	13.29	21600
NASTRAN		14.79	2.057	13.35	1728
Ref. [52] - Numerical		——	——	13.70	510
Ref. [53] - Numerical		——	——	11.10	——
Ref. [53] - Experimental		——	——	12.50	——

Table 4
Static aeroelastic response and divergence speed for a composite $[-60_2, 90]_S$ laminate wing plate. Wing geometry: rectangular planform; $\Lambda = 0°$; $c = 76.2$ mm; $b/2 = 305$ mm; overall thickness $\zeta = 0.804$ mm. Ply material properties: *Material 2* in Table 1. Aerodynamic flow: $\alpha = 1°$; aeroelastic response computed for $V_\infty = 10$ m/s.

Theory	p	u_z [mm]	Δu_z [mm]	V_D [m/s]	DOF
BT_1	2	8.473	1.743	14.00	360
	3	8.889	1.828	13.81	480
	4	8.895	1.829	13.81	600
	5	8.895	1.830	13.81	720
BT_3	2	8.673	1.852	13.76	1440
	3	9.167	1.958	13.56	1920
	4	9.180	1.962	13.55	2400
	5	9.180	1.962	13.55	2880
PT_1	2	8.703	1.852	13.76	2700
	3	9.243	1.965	13.55	4800
	4	9.287	1.976	13.53	7500
	5	9.379	2.003	13.49	10800
PT_3	2	8.700	1.851	13.76	5400
	3	9.242	1.965	13.55	9600
	4	9.285	1.975	13.53	15000
	5	9.214	1.952	13.57	21600
NASTRAN		9.170	1.950	13.57	1728
Ref. [52] - Numerical		——	——	13.80	510
Ref. [53] - Numerical		——	——	11.50	——
Ref. [53] - Experimental		——	——	11.70	——

for selected values of the sweep angle Λ. The color-plot of the deformed surface, obtained form the DG solution, is superimposed on the solution computed with NASTRAN, sketched in black continuous lines; also in this case, analogously to what observed for the single-layer wing plate, fully satisfying match is observed.

Eventually, Fig. 10 reports the divergence speed V_D as a function of the sweep angle Λ for wing plates with different stacking sequences, as computed employing the same DG scheme described above, i.e. 2×4 DG_5 PT_1 elements coupled with an aerodynamic 10×40 VLM grid. The wing geometry is the same as that considered in Figs. 8–9 and the same aerodynamic angle $\alpha = 1°$ is considered. Also in this case, a fully satisfactory match between the proposed and the benchmark solution is recorded for all the considered combinations of sweep angle and stacking sequence.

7. Discussion and future developments

This work has successfully extended a DG-VLM framework previously developed for isotropic structures [36] to the static aeroelastic analysis of general composite wings. The performed tests have validated its accuracy and confirmed its robustness for the analysis of both single- and multi-layer configurations. Thanks to the features of the underlying DG formulation, the framework provides several advantages over alternative approaches, which include: flexibility in selecting the desired order of interpolation for the problem fields, including the possibility of using different orders of approximation over different mesh elements; simplification in the implementation of parallel computing algorithms for the assembly of the discrete operators, which may be relevant for tackling large scale problems; easier coupling with other numerical methods for multi-field analysis, which is here exploited for implementing the fluid–structure interface. Such advantages come at a cost of a more complex mathematical formulation with respect to standard FEM, as shown, for instance, by the presence of the boundary-integral terms in the bilinear form $B(\boldsymbol{v}, \boldsymbol{u}^h)$ given in Eq. (12).

A few additional comments about the developed framework are noteworthy, for complementing the discussion of the above results. Focusing on the structural aspects:

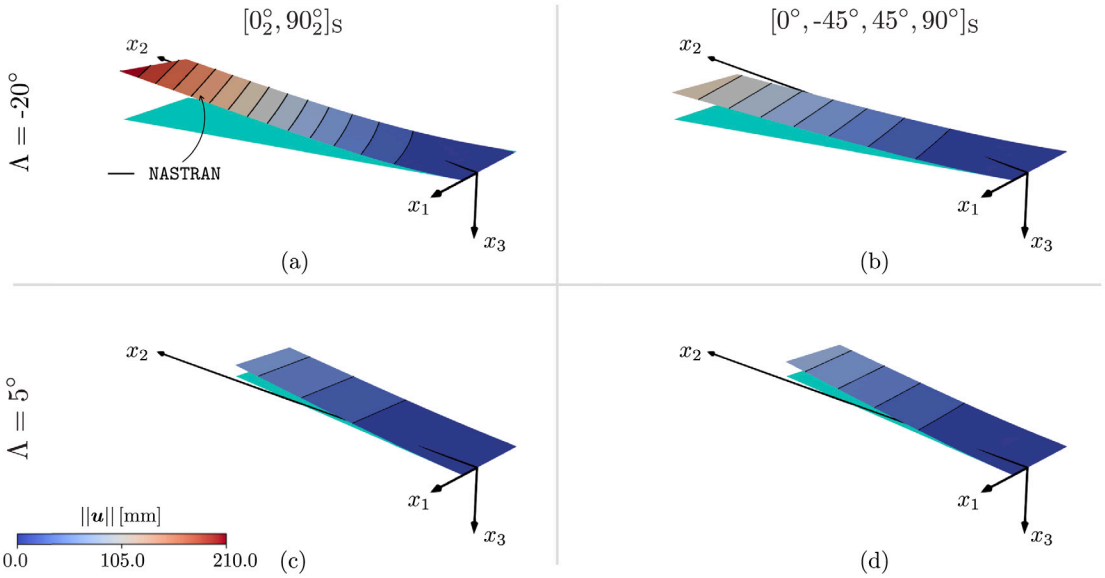

Fig. 9. Deformed configurations of the considered multi-layer wing plates for selected sweep angles. Wing geometry: $c = 1\,\text{m}$, $b/2 = 4\,\text{m}$, $\zeta/c = 0.01$. Aerodynamic flow: $\alpha = 1°$, $V_\infty = 10\,\text{m/s}$. The color-graded plots correspond to the solution computed using the proposed DG scheme; the black continuous lines represent the solution provided by the NASTRAN FE analysis.

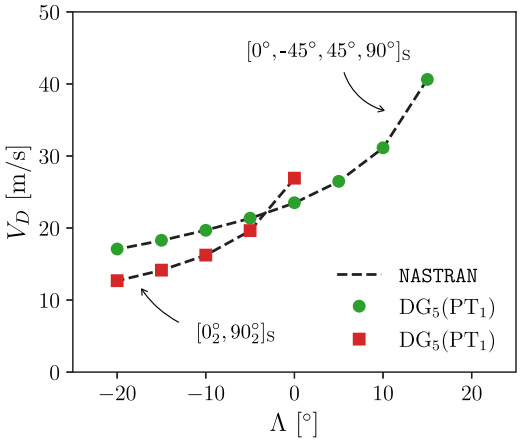

Fig. 10. Static divergence speed V_D for multi-layer composite wing plates as a function of the sweep angle Λ and stacking sequence. Wing geometry: $c = 1\,\text{m}$, $b/2 = 4\,\text{m}$, $\zeta/c = 0.01$. AoA $\alpha = 1°$. DG solution: (2×4) DG_5 PT_1 plate elements. FE solution: NASTRAN, 10×40 shell elements. Aerodynamic grid: 10×40 elements for both the structural methods (DG is coupled with VLM, FEM is coupled with DLM). *Note:* no divergence speed has been detected for $\Lambda > 0°$ for the $[0_2^\circ, 90_2^\circ]_S$ configuration, with neither method.

- Tuning the order of approximation throughout the structural domain allows minimizing the number of degrees of freedom needed to achieve convergence of quantities relevant for aeroelastic problems, such as the wing tip rotation or the divergence speed. This is demonstrated by the convergence analyses presented in the paper, which show how high-order in-plane approximations enable much faster convergence than low-order in-plane approximations, while, as expected, a low-order through-the-thickness approximation does not affect the accuracy of the solution, especially for high-aspect ratio wings.
- When $n \geq 2$, the employed models employ a fully three-dimensional constitutive law, as in Eq. (8), and it may be observed that a PT_n built using a single element along the chord coincides in fact with a BT_n, as long as both models are subsequently combined with a DG_p formulation with $p = n$.
- In either BTs or PTs, the grids are always chosen to feature one element throughout the wing thickness; as a consequence, these models can be considered as equivalent single-layer beam or plate models that automatically satisfy the inter-laminar continuity. Nevertheless, the present framework allows introducing multiple elements along the thickness and, as such, considering layer-wise kinematic approximations; in this case, the inter-laminar continuity could be enforced in a strong form by condensation of the degrees of freedom, or in a weak sense by a DG-based approach.
- The same shear factor is employed for both beam and plate (first-order) models, regardless of the considered stacking sequence; a more precise evaluation of the shear factors could also be included in the present framework, differentiating between beam and plate models as well as accounting for different stacking sequences. However, as demonstrated by the numerical results, these first-order models employing a constant shear factor provide satisfactorily accurate results.
- The difference between the solution obtained by solving Eq. (20) or the solution obtained by solving the linearized version of Eq. (20), i.e., Eq. (24), has been investigated in Ref. [36] for wing structures with isotropic constitutive behavior. It was found that two solutions differ only for very high-aspect ratio wings, which however would likely require large-strain structural models to accurately capture their mechanical response. Such considerations hold also for composite multi-layer wings.

Eventually, building on the validated results, a few directions for further developments and investigation can be identified. First, along the lines of the last comment reported above, a first interesting development could be addressed at enabling large-strain kinematics in the structural model, which would open to the possibility of investigating highly flexible high-aspect ratio wing configurations [3]. Additionally, the method could be extended to consider more complex structural and/or material architectures, e.g. *variable angle tow* composites, with more realistic representations of stiffeners, ribs and/or cut-outs [44,45,47]. The inclusion of structural dynamics and unsteady aerodynamics, e.g. with unsteady VLM [4] or DLM [54] would enable the analysis of aeroelastic flutter. Moreover, considering the capability of higher-order models to represent the presence and effects of damage [55,56], the framework could be extended to numerically investigate the potential

hazard that structural damage may pose upon altering the divergence and flutter boundaries of the wing [57]. Finally, from the flight mechanics perspective, the present method could also be extended by introducing the interaction of multiple lifting surfaces and/or the consideration of different flight conditions, which would allow capturing the aeroelastic response of a whole aircraft [4].

Conclusions

In this contribution a discontinuous Galerkin structural model has been combined with the vortex lattice method to develop a framework for the static aeroelastic analysis of either single- or multi-layer composite wing plates. Thanks to the features of the underlying DG formulation, the method offers variable-order accuracy and seamless coupling with the aerodynamic method for the aeroelastic analysis. The numerous computational tests performed have demonstrated that the method always provides accurate aeroelastic solutions and in some cases faster rates of convergence with respect to the number of degrees of freedom. The study confirms that the proposed tool may be useful in preliminary aeroelastic assessments during early conceptual design stages.

CRediT authorship contribution statement

Dario Campagna: Writing – original draft, Visualization, Validation, Software, Investigation, Data curation, Conceptualization. **Vincenzo Gulizzi:** Writing – review & editing, Visualization, Supervision, Software, Methodology, Funding acquisition, Formal analysis, Data curation, Conceptualization. **Ivano Benedetti:** Writing – review & editing, Visualization, Validation, Supervision, Methodology, Investigation, Formal analysis, Conceptualization.

Declaration of competing interest

We have no known competing financial interests or personal relationships that could have appeared to influence the work reported in this paper.

Acknowledgments

VG acknowledges the support by the European Union – Next Generation EU - PNRR M4 - C2 - investimento 1.1: Fondo per il Programma Nazionale di Ricerca e Progetti di Rilevante Interesse Nazionale (PRIN) - PRIN 2022 cod.2022AALLEC dal titolo “Hydrodynamic devices for micro-particle trapping and vibrational energy harvesting (HYDRA)” CUP B53D23005770006.

Appendix A. DG stiffness matrix

The stiffness matrix $\mathbf{K}_\mathrm{S}$ appearing in Eq. (16) is a block sparse matrix consisting of diagonal terms $\mathbf{K}_\mathrm{S}^e$, for $e = 1, \dots, N_e$, being N_e the total number of elements, and off-diagonal terms $\mathbf{K}_\mathrm{S}^{e,e'}$ which are different from zero only when the elements $\mathscr{D}^e$ and $\mathscr{D}^{e'}$ share an interface. Upon recalling that the stiffness matrix is obtained from the bilinear form $B(\boldsymbol{v}, \boldsymbol{u}^h)$ given in Eq. (12), it is possible to show, see, e.g., Ref. [50], the matrix $\mathbf{K}_\mathrm{S}^e$ has the following expression

$$\begin{aligned}\mathbf{K}_\mathrm{S}^e \equiv & \int_{\mathscr{D}^e} \frac{\partial \boldsymbol{B}^{e\intercal}}{\partial x_k} \boldsymbol{c}_{kl}^e \frac{\partial \boldsymbol{B}^e}{\partial x_l} \mathrm{d}V - \frac{1}{2} \int_{\mathscr{F}^e} \left(n_k^e \boldsymbol{B}^{e\intercal} \boldsymbol{c}_{kl} \frac{\partial \boldsymbol{B}^e}{\partial x_l} + \frac{\partial \boldsymbol{B}^{e\intercal}}{\partial x_k} \boldsymbol{c}_{kl} \boldsymbol{B}^e n_l^e \right) \mathrm{d}S \\ & + \int_{\mathscr{F}^e} \mu \boldsymbol{B}^{e\intercal} \boldsymbol{B}^e \mathrm{d}S + \\ & - \int_{\mathscr{B}_D^e} \left(n_k^e \boldsymbol{B}^{e\intercal} \boldsymbol{c}_{kl} \frac{\partial \boldsymbol{B}^e}{\partial x_l} + \frac{\partial \boldsymbol{B}^{e\intercal}}{\partial x_k} \boldsymbol{c}_{kl} \boldsymbol{B}^e n_l^e \right) \mathrm{d}S + \int_{\mathscr{B}_D^e} \mu \boldsymbol{B}^{e\intercal} \boldsymbol{B}^e \mathrm{d}S, \end{aligned} \tag{A.1}$$

whereas the matrix $\mathbf{K}_\mathrm{S}^{e,e'}$ is obtained by

$$\mathbf{K}_\mathrm{S}^{e,e'} \equiv -\frac{1}{2} \int_{\mathscr{F}^i} \left(n_k^e \boldsymbol{B}^{e\intercal} \boldsymbol{c}_{kl} \frac{\partial \boldsymbol{B}^{e'}}{\partial x_l} + \frac{\partial \boldsymbol{B}^{e\intercal}}{\partial x_k} \boldsymbol{c}_{kl} \boldsymbol{B}^{e'} n_l^{e'} \right) \mathrm{d}S - \int_{\mathscr{F}^i} \mu \boldsymbol{B}^{e\intercal} \boldsymbol{B}^{e'} \mathrm{d}S. \tag{A.2}$$

Appendix B. DG-VLM aeroelastic coupling matrices

The matrix $\partial \mathbf{b} / \partial \mathbf{X}_\mathrm{S}|_0$ is a sparse matrix linking the deformation of the unit normal of the wing surface to the structural degrees of freedom. Given a generic ith aerodynamic control point $\boldsymbol{x}_c^i$ located within the eth element, the derivative of the ith term b_i of the vector $\mathbf{b}$ with respect to the jth structural degree of freedom $X_j^{e,k}$ associated to the kth displacement component has the following expression

$$\left. \frac{\partial b_i}{\partial X_j^{e,k}} \right|_0 \equiv \sum_{q=1}^{3} \psi_q^i \left. \frac{\partial B_j^e}{\partial x_q} \right|_{\boldsymbol{x}_c^i} \hat{n}_k^i, \quad \text{being} \quad \psi_q^i \equiv \left(V_{\infty q} - \hat{n}_q^i \boldsymbol{V}_\infty \cdot \hat{\boldsymbol{n}}^i \right), \tag{B.1}$$

where B_j^e has been introduced in Eq. (5) and no implicit summation is intended. Note that $\partial b_i / \partial X_j^{e,k}$ is zero if the ith aerodynamic control point does not fall within the eth element.

On the other hand, the matrix $\partial \mathbf{F} / \partial \mathbf{\Gamma}|_0$ appearing in Eq. (22) is obtained using Eq. (19). In particular, given a jth ring vortex with the associated midpoint $\boldsymbol{x}_m^j$ of the leading segment, the derivative of the structural right-hand side $F_i^{e,k}$ associated with the kth component of the external forces acting on the eth element with respect to the circulation Γ^j is obtained as

$$\left. \frac{\partial F_i^{e,k}}{\partial \Gamma_j} \right|_0 \equiv B_i^e(\boldsymbol{x}_m^j) \rho_\infty [\boldsymbol{v}(\boldsymbol{x}_m^j) \times \boldsymbol{l}^j]_k s^j, \tag{B.2}$$

where $[\bullet]_k$ indicates the kth component of the vector $\bullet$ and s^j is $+1$ or -1 depending on how the circulation Γ^j appears in the definition of $\widetilde{\Gamma}^j$ in Eq. (19).

Data availability

Data will be made available on request.

References

[1] Arena A, Lacarbonara W, Valentine D, Marzocca P. Aeroelastic behavior of long-span suspension bridges under arbitrary wind profiles. J Fluids Struct 2014;50:105–19. http://dx.doi.org/10.1016/j.jfluidstructs.2014.06.018, URL https://www.sciencedirect.com/science/article/pii/S0889974614001364.

[2] Zou L, Li F, Song J, Shi T, Liang S, Mercan O. Investigation of torsional aeroelastic effects on high-rise buildings using forced vibration wind tunnel tests. J Wind Eng Ind Aerodyn 2020;200:104158. http://dx.doi.org/10.1016/j.jweia.2020.104158, URL https://www.sciencedirect.com/science/article/pii/S0167610520300684.

[3] Palacios R, Murua J, Cook R. Structural and aerodynamic models in nonlinear flight dynamics of very flexible aircraft. AIAA J 2010;48(11):2648–59. http://dx.doi.org/10.2514/1.J050513.

[4] Murua J, Palacios R, Graham JMR. Applications of the unsteady vortex-lattice method in aircraft aeroelasticity and flight dynamics. Prog Aerosp Sci 2012;55:46–72. http://dx.doi.org/10.1016/j.paerosci.2012.06.001, URL https://www.sciencedirect.com/science/article/pii/S0376042112000620.

[5] Afonso F, Vale J, Éder Oliveira Lau F, Suleman A. A review on non-linear aeroelasticity of high aspect-ratio wings. Prog Aerosp Sci 2017;89:40–57. http://dx.doi.org/10.1016/j.paerosci.2016.12.004, URL https://www.sciencedirect.com/science/article/pii/S037604211630077X.

[6] Casoni M, Benini E. A review of computational methods and reduced order models for flutter prediction in turbomachinery. Aerospace 2021;8(9). http://dx.doi.org/10.3390/aerospace8090242, URL https://www.mdpi.com/2226-4310/8/9/242.

[7] De Marqui Carlos J, Vieira WGR, Erturk A, Inman DJ. Modeling and analysis of piezoelectric energy harvesting from aeroelastic vibrations using the doublet-lattice method. J Vib Acoust 2010;133(1):011003.

[8] Carrión M, Steijl R, Woodgate M, Barakos G, Munduate X, Gomez-Iradi S. Aeroelastic analysis of wind turbines using a tightly coupled cfd–csd method. J Fluids Struct 2014;50:392–415. http://dx.doi.org/10.1016/j.jfluidstructs.2014.06.029, URL https://www.sciencedirect.com/science/article/pii/S0889974614001546.

[9] Wang L, Liu X, Kolios A. State of the art in the aeroelasticity of wind turbine blades: Aeroelastic modelling. Renew Sustain Energy Rev 2016;64:195–210. http://dx.doi.org/10.1016/j.rser.2016.06.007, URL https://www.sciencedirect.com/science/article/pii/S1364032116302234.

[10] Guma G, Bangga G, Lutz T, Krämer E. Aeroelastic analysis of wind turbines under turbulent inflow conditions. Wind Energy Sci 2021;6(1):93–110. http://dx.doi.org/10.5194/wes-6-93-2021, URL https://wes.copernicus.org/articles/6/93/2021/.

[11] Liu Y, Xiao Q, Incecik A, Peyrard C. Aeroelastic analysis of a floating offshore wind turbine in platform-induced surge motion using a fully coupled cfd-mbd method. Wind Energy 2019;22(1):1–20. http://dx.doi.org/10.1002/we.2265, URL https://onlinelibrary.wiley.com/doi/abs/10.1002/we.2265.

[12] Guo S, Cheng W, Cui D. Aeroelastic tailoring of composite wing structures by laminate layup optimization. AIAA J 2006;44(12):3146–50. http://dx.doi.org/10.2514/1.20166.

[13] Werter N, De Breuker R. A novel dynamic aeroelastic framework for aeroelastic tailoring and structural optimisation. Compos Struct 2016;158:369–86. http://dx.doi.org/10.1016/j.compstruct.2016.09.044, URL https://www.sciencedirect.com/science/article/pii/S0263822316318669.

[14] Scott S, Capuzzi M, Langston D, Bossanyi E, McCann G, Weaver PM, et al. Effects of aeroelastic tailoring on performance characteristics of wind turbine systems. Renew Energy 2017;114:887–903. http://dx.doi.org/10.1016/j.renene.2017.06.048, URL https://www.sciencedirect.com/science/article/pii/S0960148117305530.

[15] Ma Y, Elham A. Designing high aspect ratio wings: A review of concepts and approaches. Prog Aerosp Sci 2024;145:100983. http://dx.doi.org/10.1016/j.paerosci.2024.100983, URL https://www.sciencedirect.com/science/article/pii/S0376042124000095.

[16] Patil M, Hodges D. On the importance of aerodynamic and structural geometrical nonlinearities in aeroelastic behavior of high-aspect-ratio wings. J Fluids Struct 2004;19(7):905–15. http://dx.doi.org/10.1016/j.jfluidstructs.2004.04.012, URL https://www.sciencedirect.com/science/article/pii/S0889974604000738.

[17] hui Zhao Y, yan Hu H. Structural modeling and aeroelastic analysis of high-aspect-ratio composite wings. Chin J Aeronaut 2005;18(1):25–30. http://dx.doi.org/10.1016/S1000-9361(11)60278-1, URL https://www.sciencedirect.com/science/article/pii/S1000936111602781.

[18] Koohi R, Shahverdi H, Haddadpour H. Nonlinear aeroelastic analysis of a composite wing by finite element method. Compos Struct 2014;113:118–26. http://dx.doi.org/10.1016/j.compstruct.2014.03.012, URL https://www.sciencedirect.com/science/article/pii/S0263822314001159.

[19] Filippi M, Carrera E. Aerodynamic and mechanical hierarchical aeroelastic analysis of composite wings. Mech Adv Mater Struct 2016;23(9):997–1004. http://dx.doi.org/10.1080/15376494.2015.1121561.

[20] Bhardwaj MK, Kapania RK, Reichenbach E, Guruswamy GP. Computational fluid dynamics/computational structural dynamics interaction methodology for aircraft wings. AIAA J 1998;36(12):2179–86. http://dx.doi.org/10.2514/2.342.

[21] Maute K, Nikbay M, Farhat C. Coupled analytical sensitivity analysis and optimization of three-dimensional nonlinear aeroelastic systems. AIAA J 2001;39(11):2051–61. http://dx.doi.org/10.2514/2.1227.

[22] Ilie M. A fully-coupled cfd/csd computational approach for aeroelastic studies of helicopter blade-vortex interaction. Appl Math Comput 2019;347:122–42. http://dx.doi.org/10.1016/j.amc.2018.10.069, URL https://www.sciencedirect.com/science/article/pii/S0096300318309433.

[23] Medeiros RR, Cesnik CES, Coetzee EB. Computational aeroelasticity using modal-based structural nonlinear analysis. AIAA J 2020;58(1):362–71. http://dx.doi.org/10.2514/1.J058593.

[24] Sayed M, Bucher P, Guma G, Lutz T, Wüchner R. Aeroelastic simulations based on high-fidelity cfd and csd models. In: Handbook of wind energy aerodynamics. 2022, p. 1–76. http://dx.doi.org/10.1007/978-3-030-05455-7_22-1.

[25] Grifò M, Da Ronch A, Benedetti I. A computational aeroelastic framework based on high-order structural models and high-fidelity aerodynamics. Aerosp Sci Technol 2023;132:108069. http://dx.doi.org/10.1016/j.ast.2022.108069, URL https://www.sciencedirect.com/science/article/pii/S127096382200743X.

[26] Grifò M, Gulizzi V, Milazzo A, Da Ronch A, Benedetti I. High-fidelity aeroelastic transonic analysis using higher-order structural models. Compos Struct 2023;321:117315. http://dx.doi.org/10.1016/j.compstruct.2023.117315, URL https://www.sciencedirect.com/science/article/pii/S026382232300661X.

[27] Thelen AS, Bryson DE, Stanford BK, Beran PS. Multi-fidelity gradient-based optimization for high-dimensional aeroelastic configurations. Algorithms 2022;15(4). http://dx.doi.org/10.3390/a15040131, URL https://www.mdpi.com/1999-4893/15/4/131.

[28] Varello A, Demasi L, Carrera E, Giunta G. An improved beam formulation for aeroelastic applications. Collection of technical papers - AIAA/ASME/ASCE/AHS/ASC structures. In: Structural dynamics and materials conference. 2010, http://dx.doi.org/10.2514/6.2010-3032.

[29] Varello A, Carrera E, Demasi L. Vortex lattice method coupled with advanced one-dimensional structural models. J Aeroelast Struct Dyn 2011;2(2).

[30] Carrera E, Varello A, Demasi L. A refined structural model for static aeroelastic response and divergence of metallic and composite wings. CEAS Aeronaut J 2013;4(2):175–89.

[31] Petrolo M. Flutter analysis of composite lifting surfaces by the 1d carrera unified formulation and the doublet lattice method. Compos Struct 2013;95:539–46. http://dx.doi.org/10.1016/j.compstruct.2012.06.021, URL https://www.sciencedirect.com/science/article/pii/S0263822312003108.

[32] Xie C, Wang L, Yang C, Liu Y. Static aeroelastic analysis of very flexible wings based on non-planar vortex lattice method. Chin J Aeronaut 2013;26(3):514–21. http://dx.doi.org/10.1016/j.cja.2013.04.048, URL https://www.sciencedirect.com/science/article/pii/S100093611300099X.

[33] Koohi R, Shahverdi H, Haddadpour H. Nonlinear aeroelastic analysis of a composite wing by finite element method. Compos Struct 2014;113:118–26. http://dx.doi.org/10.1016/j.compstruct.2014.03.012, URL https://www.sciencedirect.com/science/article/pii/S0263822314001159.

[34] Rajpal D, Gillebaart E, De Breuker R. Preliminary aeroelastic design of composite wings subjected to critical gust loads. Aerosp Sci Technol 2019;85:96–112. http://dx.doi.org/10.1016/j.ast.2018.11.051, URL https://www.sciencedirect.com/science/article/pii/S1270963818303948.

[35] Vindigni CR, Mantegna G, Esposito A, Orlando C, Alaimo A. An aeroelastic beam finite element for time domain preliminary aeroelastic analysis. Mech Adv Mater Struct 2023;30(5):1064–72. http://dx.doi.org/10.1080/15376494.2022.2124333.

[36] Gulizzi V, Benedetti I. Computational aeroelastic analysis of wings based on the structural discontinuous galerkin and aerodynamic vortex lattice methods. Aerosp Sci Technol 2024;144:108808. http://dx.doi.org/10.1016/j.ast.2023.108808, URL https://www.sciencedirect.com/science/article/pii/S1270963823007046.

[37] Xie C, An C, Yi L, Chao Y. Static aeroelastic analysis including geometric nonlinearities based on reduced order model. Chin J Aeronaut 2017;30. http://dx.doi.org/10.1016/j.cja.2016.12.031.

[38] Kou J, Zhang W. A hybrid reduced-order framework for complex aeroelastic simulations. Aerosp Sci Technol 2019;84:880–94. http://dx.doi.org/10.1016/j.ast.2018.11.014, URL https://www.sciencedirect.com/science/article/pii/S1270963818316894.

[39] Li D, Da Ronch A, Chen G, Li Y. Aeroelastic global structural optimization using an efficient cfd-based reduced order model. Aerosp Sci Technol 2019;94:105354. http://dx.doi.org/10.1016/j.ast.2019.105354, URL https://www.sciencedirect.com/science/article/pii/S1270963819311046.

[40] Carrera E, Cinefra M, Petrolo M, Zappino E. Finite element analysis of structures through unified formulation. John Wiley & Sons; 2014.

[41] Reddy JN. Mechanics of laminated composite plates and shells: theory and analysis. CRC Press; 2003.

[42] Jones RM. Mechanics of composite materials. CRC Press; 2018.

[43] Gulizzi V, Benedetti I, Milazzo A. High-order accurate beam models based on discontinuous Galerkin methods. Aerotecn Missili Spazio 2023;1–16.

[44] Gulizzi V, Benedetti I, Milazzo A. An implicit mesh discontinuous Galerkin formulation for higher-order plate theories. Mech Adv Mater Struct 2020;27(17):1494–508.

[45] Gulizzi V, Benedetti I, Milazzo A. A high-resolution layer-wise discontinuous Galerkin formulation for multilayered composite plates. Compos Struct 2020;242:112137.

[46] Guarino G, Milazzo A, Gulizzi V. Equivalent-single-layer discontinuous Galerkin methods for static analysis of multilayered shells. Appl Math Model 2021;98:701–21.

[47] Guarino G, Gulizzi V, Milazzo A. High-fidelity analysis of multilayered shells with cut-outs via the discontinuous Galerkin method. Compos Struct 2021;276:114499.

[48] Guarino G, Gulizzi V, Milazzo A. Accurate multilayered shell buckling analysis via the implicit-mesh discontinuous Galerkin method. AIAA J 2022;60(12):6854–68.

[49] Gulizzi V, Benedetti I, Milazzo A. High-order accurate transient and free-vibration analysis of plates and shells. J Sound Vib 2024;587:118479. http://dx.doi.org/10.1016/j.jsv.2024.118479, URL https://www.sciencedirect.com/science/article/pii/S0022460X24002426.

[50] Gulizzi V, Benedetti I, Milazzo A. Discontinuous galerkin methods for solids and structures. In: Aliabadi MHF, Soboyejo WO, editors. Comprehensive structural integrity. 2nd ed. Oxford: Elsevier; 2023, p. 348–77. http://dx.doi.org/10.1016/B978-0-12-822944-6.00024-4, URL https://www.sciencedirect.com/science/article/pii/B9780128229446000244.

[51] Katz J, Plotkin A. Low-speed aerodynamics. Cambridge aerospace series, 2nd ed. Cambridge University Press; 2001, http://dx.doi.org/10.1017/CBO9780511810329.

[52] Kameyama M, Fukunaga H. Optimum design of composite plate wings for aeroelastic characteristics using lamination parameters. Comput Struct 2007;85(3–4):213–24.

[53] Hollowell SJ, Dugundji J. Aeroelastic flutter and divergence of stiffness coupled, graphite/epoxy cantilevered plates. J Aircraft 1984;21(1):69–76.

[54] Albano E, Rodden WP. A doublet-lattice method for calculating lift distributions on oscillating surfaces in subsonic flows. AIAA J 1969;7(2):279–85. http://dx.doi.org/10.2514/3.5086.

[55] Campagna D, Milazzo A, Benedetti I, Oliveri V. A non-linear ritz method for progressive failure analysis of variable angle tow composite laminates. Mech Adv Mater Struct 2023;30(5):995–1008. http://dx.doi.org/10.1080/15376494.2022.2134951.

[56] Campagna D, Oliveri V, Benedetti I. An adaptive ritz formulation for progressive damage modelling in variable angle tow composite plates. Compos Struct 2024;331:117915. http://dx.doi.org/10.1016/j.compstruct.2024.117915, URL https://www.sciencedirect.com/science/article/pii/S0263822324000436.

[57] Hoseini HS, Hodges DH. Aeroelastic stability analysis of damaged high-aspect-ratio composite wings. J Aircr 2019;56(5):1794–808. http://dx.doi.org/10.2514/1.C035098.